FlatChem 2 (2017) 15–37

Contents lists available at ScienceDirect

FlatChem

journal homepage: www.elsevier.com/locate/flatc

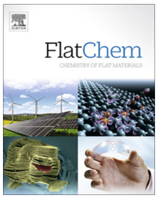

Liquid-phase exfoliation of black phosphorus and its applications

Shenghuang Lin [1], Yingsan Chui [1], Yanyong Li, Shu Ping Lau *

Department of Applied Physics, The Hong Kong Polytechnic University, Hung Hom, Kowloon, Hong Kong, China

ARTICLE INFO

Article history:
Received 17 March 2017
Revised 28 March 2017
Accepted 28 March 2017
Available online 5 April 2017

Keywords:
Black phosphorus
Two-dimensional materials
Solution exfoliation
Energy materials

ABSTRACT

Interest in two-dimensional (2D) materials is growing exponentially across various scientific and engineering disciplines owing to their fascinating electrical, optical, chemical, and thermal properties. As one of the newest members in the 2D nanomaterial family, black phosphorus (BP), has recently attracted much attention all over the world and shown great potential in novel nanoelectronics owing to its direct and narrow bandgap. Regarding to the scale production of BP and its related electronic devices, liquid-phase exfoliation reveals superior advances when compared with mechanical exfoliation. Remarkably, liquid-phase exfoliated BP flakes and quantum dots (QDs) exhibit exciting properties in electronic, energy storage, sensors, solar cells, photothermal effect, cancer theranostics and photonic devices. In this article, we discuss the exfoliation of BP in diverse solvents and extend the topic from BP flakes to QDs and summarize the significant advances recently made. We also outline future prospects of solution exfoliated BP nanomaterials, and comment on the challenges that need to be overcome for future applications.

Contents

---

* Corresponding author.
E-mail address: apsplau@polyu.edu.hk (S.P. Lau).

[1] These authors are contributed equally to this work.

http://dx.doi.org/10.1016/j.flatc.2017.03.001
2452-2627/

Introduction

The evolution of materials science plays an important role in the development of human society. The discovery of graphene [1–6], as a superstar in materials science, has obviously attracted great attention around the world and created tremendous impact in many fields. It is indeed enhanced the knowledge of layered two-dimensional (2D) materials in the past few years. It is no doubt that the research of layered 2D materials has been in the frontier of materials science [5,7]. To explore the unique properties of 2D materials, the first step is to isolate them from the bulk into few-layer or even single-layer form through mechanical or liquid-phase exfoliation process. The exfoliated 2D materials typically have weak van der Waals or electrostatic out-of-plane interactions and strong covalent or ionic in-plane bonds [8]. There are many kinds of 2D materials, which can be isolated from their bulk counterparts, e.g., graphene, GaSe, MoS_2, MnO_2 and black phosphorus (BP) [9–12]. Due to their interesting properties, 2D materials have been explored carefully when thinned down to atomic layer scale and reveal significant changes in the mechanical, physical and chemical properties. For example, the bandgap of MoS_2, a typical member belonging to the family of transition metal dichalcogenides (TMDs), varies from 1.29 eV to 1.8 eV when the thickness of bulk is thinned down to single-layer [13]. It has great potential applications in photovoltaics [14–16], photodetectors [17,18], and light emitters [19]. In addition to TMDs and graphene, scientists also pay much attention to explore new 2D semiconductors. Interestingly, the rediscovering of BP, a rare and stable allotrope of phosphorus, has excited materials scientists to make BP as a promising candidate for complementing graphene's deficiencies. Remarkably, both experimental and theoretical results revealed that BP possesses a direct bandgap ranging from 0.3 eV (bulk) to 2.0 eV (monolayer) [20], which can bridge the gap between zero-gap graphene and relatively large bandgap TMDs for infrared photonics and optoelectronics [21,22]. To make full use of the excellent physical and optical properties of BP, many efforts have been devoted to enlarging the size of BP flakes or films. For instance, BP film with lateral size of 4 mm can be prepared by converting a red phosphorus film at high-pressure [23]; and large-area amorphous BP film with a mobility of $14\ cm^2\ V^{-1}\ s^{-1}$ can be obtained through Pulsed Laser Deposition (PLD) technique [24]. In terms of the stability of few-layer BP in ambient air, advancements have been made to enhance the stability of BP. Typically, an encapsulation of BN (boron nitride) [25,26], Al_2O_3 [27,28] or PMMA [29] onto BP surface could effectively improve its stability. Although room temperature hole mobilities of $\sim 1000\ cm^2\ V^{-1}\ s^{-1}$ with on/off ratios of $\sim 10^3 - 10^5$ can be achieved in mechanically exfoliated few-layer BP based field effect transistors (FETs) [30], such mechanical exfoliation technique suffers from low yield and a low production rate, which is not scalable for practical applications. As compared, solution-processed electronic devices are usually preferred due to its low cost, large area, flexibility and convenient materials integration [31]. Therefore, one possible solution is to exfoliate BP in liquid to give large scale dispersion of nanosheets to extend the application of BP. Herein, we critically review the recent advances in the preparation and applications of liquid-phase exfoliated BP. This review is an account of the current status of science in liquid-phase exfoliation of BP, with special attention paid to applications that have emerged in recent years.

Properties of black phosphorus

The allotropes of phosphorus and the electronic structure of BP

Phosphorus usually exists in various allotropes, such as gaseous, white, red, black and violet, which exhibit strikingly different properties as shown in Fig. 1 and Table 1 [32–34]. Diphosphorus (P_2) is one of the allotropes of phosphorus presenting its gaseous form through the thermolysis (cracking) of P_4 (white phosphorus) at 1100 K. Meanwhile, blue phosphorus, another unique and stable phase of phosphorus, has also been experimentally studied by *in-situ* scanning tunneling microscopy (STM). Such blue phosphorus was grown by the MBE (molecular beam epitaxy) using BP as precursor [32]. It has been revealed that the rediscovered BP normally has an orthorhombic crystal structure with five valence electrons in its outer shell [35]. In addition to the orthorhombic phase, BP also exhibits rhombohedral or simple cubic phase [35]. Similar to graphite, adjacent BP atomic layers are stacked together through weak van der Waals interaction while the single layer is formed by sp^3 phosphorus atoms through covalently bonding. Owing to the sp^3 hybridization, each P atom is saturated and covalently bonded to three neighboring P atoms and has one lone-electron pair, leading to a quadrangular pyramid structure resembling a puckered honeycomb structure, as shown in Fig. 1, and hence results in a highly asymmetric band structure and unique in-plane anisotropic properties [36]. BP possesses different lattice constants for the armchair (4.37 Å) and zigzag edges (3.31 Å), from which the unique in-plane anisotropy can be observed, e.g., a high-degree anisotropy of effective masses [37]. But the blue phosphorus has only zigzag edges with the same lattice constant of 3.28 Å, revealing the different lattice constants by comparing with BP. White phosphorus (also called yellow phosphorus), the most toxic of the allotropes of phosphorus, consists of tetrahedral P_4 molecules, in which each atom is bound to the other three atoms by a single bond (as shown in Fig. 1D). Violet phosphorus (Fig. 1E) is a form of phosphorus that can be produced by day-long annealing of red phosphorus above 550 °C. Red phosphorus, possessing polymeric chain-like structure (Fig. 1F), can be formed through heating white phosphorus to 250 °C. But the most stable allotrope among the bulk forms of phosphorus is BP. The density of BP can be calculated through counting the BP atoms in the unit cell. Here we can extract the density of $2.69\ g/cm^3$ for BP containing 8 atoms in the unit cell [30]. The crystal structure of BP can be clearly distinguished under high pressure [38] due to the anisotropic compressibility of BP induced by its asymmetric crystal structure. Generally, BP undergoes two reversible structural transitions at high pressures. The first transition occurs at around 5.5 GPa at room temperature, inducing the conversion of orthorhombic phase into rhombohedral phase and consequently resulting in the displacement of the puckered layers and a volume change. The second transition, from rhombohedral to simple cubic phase, appears when the pressure reaches 10 GPa. For ultrahigh pressure (even up to 60 GPa) [39], there is no further transition occurred, revealing the cubic phase remains stable when the pressure is higher than 10 GPa. It is worth noting that the temperature does not contribute to the phase transitions of BP [40,41]. Otherwise, the BP flakes could be decomposed at >400 °C by *in situ* TEM (transmission electron microscope) and the residual gaseous BP would be re-deposited to form amorphous phosphorus when the chamber was cooled down to room temperature [42], which provides an insight into the thermal stability of BP.

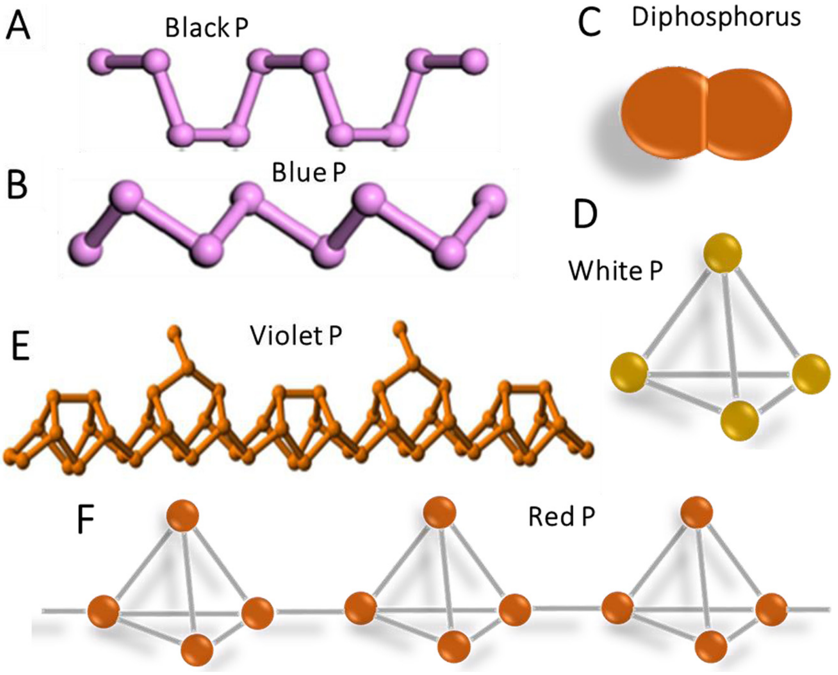

Fig. 1. Diverse allotropes of phosphorus. (A) Side view of BP [32]. Copyright © 2016, American Chemical Society. (B) Side view of blue phosphorus [32]. Copyright © 2016, American Chemical Society. (C) Gaseous form of phosphorus (named diphosphorus-P_2). (D) Unit cell of white phosphorus (P_4). (E) Side view of violet phosphorus. (F) Side view of red phosphorus.

Table 1
Typical properties of some allotropes of phosphorus [32–34].

Form	White (α)	White (β)	Violet	Black	Blue	Red	Diphosphorus (P_2-gas)
Symmetry	Body- centred cubic	Triclinic	Monoclinic	Orthorhombic	Hexagonal	Polymeric	–
Pearson symbol	–	aP24	mP84	oS8	–	–	–
Space group	I-43m	P-1No.2	P2/c No.13	Cmca No.64	–	–	–
Density (g/cm^3)	1.828	1.88	2.36	2.69	–	–	–
Bandgap (eV)	2.1	–	1.5	0.3	2	1.8	–
Refractive index	1.8244	–	2.6	2.4	–	–	–

As compared to TMDs, simulation results show that BP possesses a direct band gap regardless of its thickness (Fig. 2B) [44]. The direct band gap shows a thickness dependence such that the band gap magnitude decreases with increasing the BP layer number. Standing from the view point of band structure, there also exist a strong anisotropy of BP along the Γ–X and Γ–Y directions for all thicknesses, with the Γ–X (armchair) direction far more disperse than the Γ–Y (zigzag) direction [22,45]. This anisotropy leads to significantly different charge carrier effective masses as a function of crystallographic orientation and quasi-1D electronic properties [46], which is similar to the effect induced by in-plane anisotropy [37]. From Fig. 2A, we can also note that the VBM and CBM are composed of p_z-orbitals, resulting in the predominant p-orbital in the valence and conduction bands [43,47,48]. The variation in the magnitude of the band gap is due to the linear combination of these p_z orbitals with additional layers [47]. The featured structure of bulk and few-layer BP with direct band gaps makes it highly suitable for optoelectronic applications over a broad range of the electromagnetic spectrum, especially at the telecommunication wavelength (1550 nm).

Exfoliation of BP via sonication

Liquid-phase exfoliation refers to breaking a layered crystal into 2D materials by suspending the crystal in a "solvent" and blasting the crystal with ultrasonic energy. The general process for preparing ultrathin BP flakes by liquid-phase exfoliation involves three steps: (i) dispersion of the starting material in a liquid medium, (ii) exfoliation via sonication and (iii) centrifugation. The detailed mechanism of liquid exfoliation is schematically illustrated in Fig. 3. During the sonication process, shear forces and cavitation can be induced due to the propagation of high amplitude sonication waves acting on the surface of bulk materials, and hence shears the crystal apart [49,50]. Therefore, the strategy of using ultrasonication is an effective and scalable technique to exfoliate layered materials. The interfacial tension between the materials being exfoliated and the liquid medium should be minimized to stabilize the as-prepared 2D flakes, realizing the existence of good interactions (see Fig. 3). Thus, how to choose a moderate liquid system for the dispersion of the target materials is a key factor on the effectiveness of the methodology. Generally, several parameters like sonication time and surface tension should be considered before we reach an efficient and scalable sonication scheme.

According to solution thermodynamics, 2D materials mixed with target liquids can be considered as solutions. Then the exfoliation and dispersion of layered materials in solutions can be partially predicted by Hansen solubility parameters (HSP). Usually, there are three HSP parameters for describing the feature solute-solvent interactions of a solution or material: δ_D, δ_P and δ_H, represent the dispersion forces, polar, and hydrogen-bonding solubility

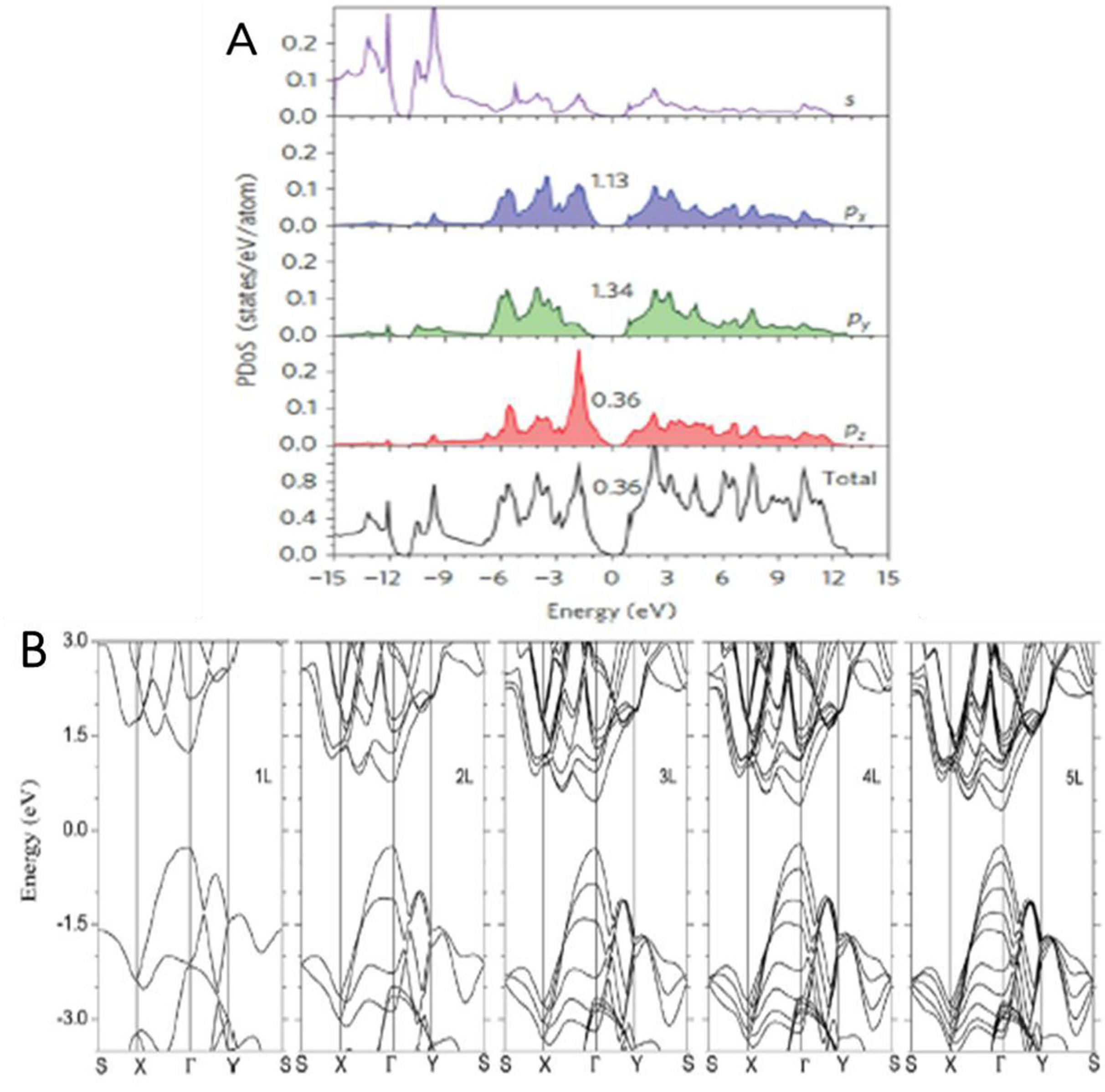

Fig. 2. (A) Projected density of states (DFT-density functional theory) of monolayer black phosphorus showing s−p orbital mixing away from the band edges and the strong p_z orbital character of the VBM and CBM [43]. Copyright © 2015, Rights Managed by Nature Publishing Group. (B) DFT calculated band structure of BP from monolayer to five-layer BP, revealing the decrease of a direct band gap magnitude with increasing layer number [44]. Copyright © 2014, Rights Managed by Nature Publishing Group.

parameters, respectively. For simplicity, we can use HSP distance R_a to find a single efficient solvent for the dispersion of 2D materials. Here, R_a value is governed by [51]

$$R_a^2 = 4(\delta_{D,solvent} - \delta_{D,solute})^2 + (\delta_{P,solvent} - \delta_{P,solute})^2 + (\delta_{H,solvent} - \delta_{H,solute})^2,$$

which implies the smaller the R_a value, the higher the expected solubility. Thus, for one material, the chosen solvents should be possessing similar surface energy when compared with the target materials for successful and high-efficiency liquid-phase exfoliation.

In order to study the appropriate solvents for efficient exfoliation of layered BP, several solvents such as alcohol, chloro-organic solvents, ketones, cyclic and organosulfur compounds were utilized. It is essential to identify suitable solvents that can promote efficient exfoliation and stabilization of BP. The solvents under study covered a wide range of surface tensions (18.4–72.7 dynes/cm) and polar interaction parameters (2.98–26.2 $MPa^{1/2}$), which guarantees careful examination of their performance in the exfoliation of BP. The detailed Hansen solubility and surface tension of several studied solvents are summarized in Table 2.

Liquid-exfoliated BP flakes were first achieved in NMP solution by Brent et al. [53] where BP flakes comprised of more than 2 layers can be obtained via one-step ultrasonication process. Since then, BP flakes were prepared in many other solvents as summarized in Table 2, including hexane, IPA, methanol, ethanol, acetone, THF, chloroform, NMF, DCB, CHP, NVP, DMSO, formamide and water [11,52,54–59]. The thickness of liquid-exfoliated BP flakes can be measured down to ~0.52 nm by drop-casting BP solution onto a transmission electron microscopy (TEM) copper grid [11]. Up to now, the reported relatively highest BP exfoliation yield in

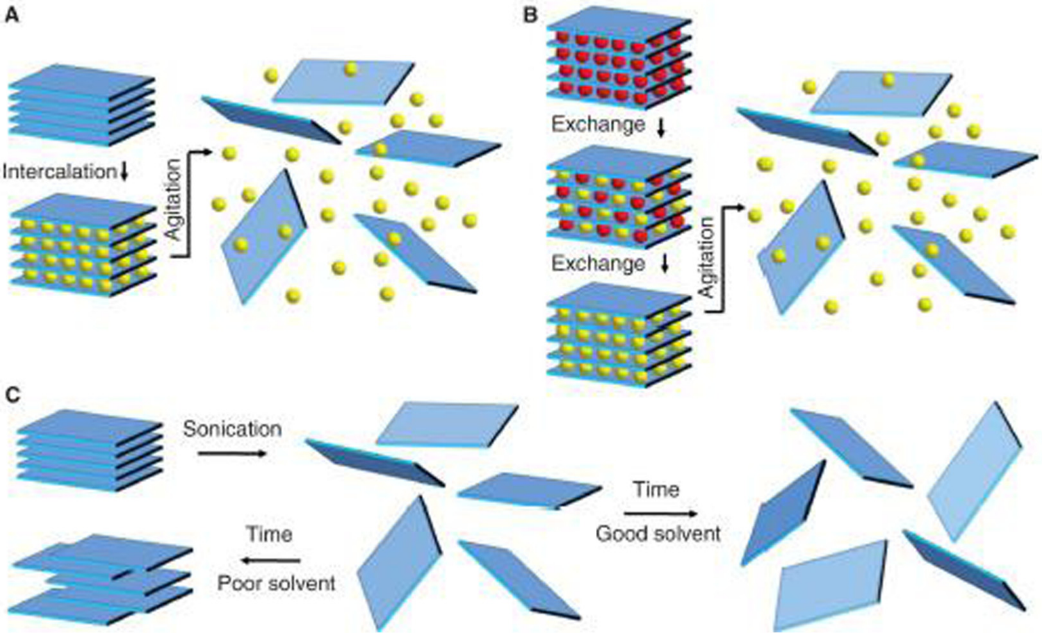

Fig. 3. Schematic illustrations of the liquid-phase exfoliation processes. (A) Ion intercalation. The interlayer attraction in the crystal is weakened by adding the ions (yellow spheres) into a liquid environment. Then, the layers can be completely separated by agitation (such as shear force, ultrasonication, or thermal energy) to form an exfoliated 2D dispersion. (B) Ion exchange. Ions (red spheres) between the layers in some layered compounds can be exchanged in a liquid environment for other larger ions (yellow spheres) to form an exfoliated dispersion. (C) Exfoliation by ultrasonication. The layered materials can be easily exfoliated in a good solvent by ultrasonication, but re-aggregated in poor solutions [9]. Copyright © 2013, American Association for the Advancement of Science.

Table 2
Summary of the exfoliation yield of BP in solvents followed by the corresponding Hansen solubility parameter and surface tension.

Solvents	Surface tension (dynes/cm)	Dispersive force (δ_D) (MPa$^{1/2}$)	Polar interaction (δ_P) (MPa$^{1/2}$)	Hydrogen bond interaction (δ_H) (MPa$^{1/2}$)	Yield (%)
Hexane	18.4	7.28	–	–	–
Iso-propyl alcohol (IPA)	21.7	7.72	2.98	8.02	16 [52]
Methanol	22.05	7.42	6	10.9	6 [52]
Ethanol	22.18	7.73	4.3	9.5	4 [52]
Acetone	22.86	7.58	5.1	3.4	~0 [52]
Tetrahydrofuran (THF)	26.4	8.2	2.8	3.9	~0 [52]
Chloroform	27.5	7.5	3.0	1.9	–
N,N-dimethylformamide (DMF)	35.2	8.52	6.7	5.5	16 [52]
1,2-Dichlorobenzene (DCB)	37.0	9.38	3.08	1.61	–
N-cyclohexyl-2-pyrrolidone (CHP)	38.79	–	–	–	–
N-vinylpyrrolidone (NVP)	40.15	16.4	9.3	5.9	–
Dimethyl sulfoxide (DMSO)	42.78	9	8	5	24 [52]
N-methyl-2-pyrrolidone (NMP)	44.6	18.0	12.3	7.2	14 [52]
Formamide	58.2	17.2	26.2	19.0	38 [52]
Pure water (H_2O) without assistance	72.7	18.1	17.1	16.9	~0 [52]

solvents can reach ~38% by formamide [52] and the concentration of BP flakes in each solvent can be sorted in the following descending order: formamide > DMSO > DMF-NMP-IPA > ethanol-methanol > acetone-THF-DI water, which can be obviously observed in Fig. 4B. According to Lambert-Beer law: $A/l = \alpha C$, where A is the absorbance intensity, l is the cell length, α is the extinction coefficient, and C is the concentration (A scales linearly with C for minor dispersions in ethanol). Once α is determined, the concentration of BP in solvents can be calculated through extracting the information from UV–vis-NIR absorption spectra as shown in Fig. 4C. By comparing the surface tension with the BP concentration in different solvents, it can be revealed that the BP exfoliation yield monotonically increases with the increase of surface tension (see Fig. 4D), which is similar to the situation in the exfoliation of graphene and TMDs [60,61]. In addition, BP flakes can also be easily obtained via ionic liquid assisted sonication [62] and shear exfoliation, as shown in Fig. 5, which provides another opportunity for preparing large-scale, and highly concentrated atomically thin BP nanosheets.

Although a solvent is capable of exfoliating a layered material, it may not suspend the material efficiently. For instance, BP flakes can be exfoliated and dispersed in ethanol but the yield is ~0 in THF [52]. Therefore, the application of Hansen solubility parameters is still limited. Interestingly, Shih et al. [64] proposed a model based on the simulation of the colloidal stability of the dispersions through measuring the attractive forces between nanosheets. The case regarding the stability of graphene suspensions revealed that the rate-determining step for aggregation of dispersed sheets is to

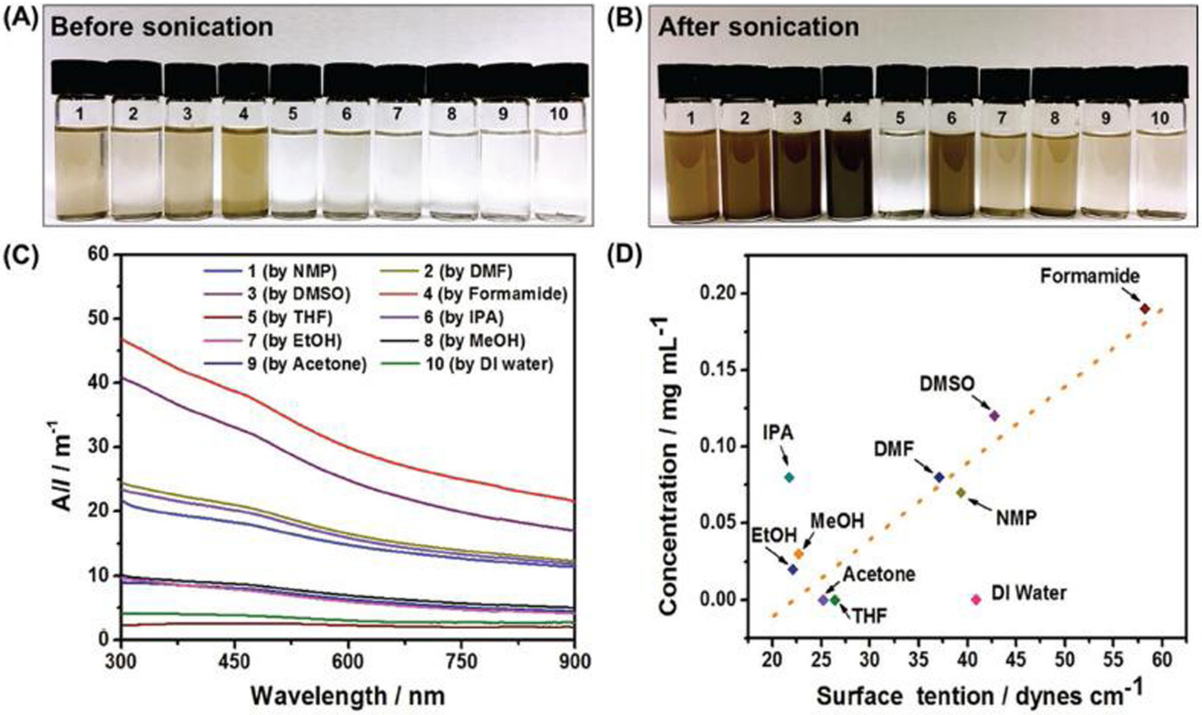

Fig. 4. Liquid-phase exfoliation of BP in different solvents through ultrasonication. Photographs of BP dispersions in different solvents (A) before sonication and (B) after sonication process. (C) Optical absorption spectrum of BP dispersions in different solvents. (D) Plot of surface tension versus BP concentration in different solvents [52]. Copyright © 2016 WILEY-VCH Verlag GmbH & Co. KGaA, Weinheim.

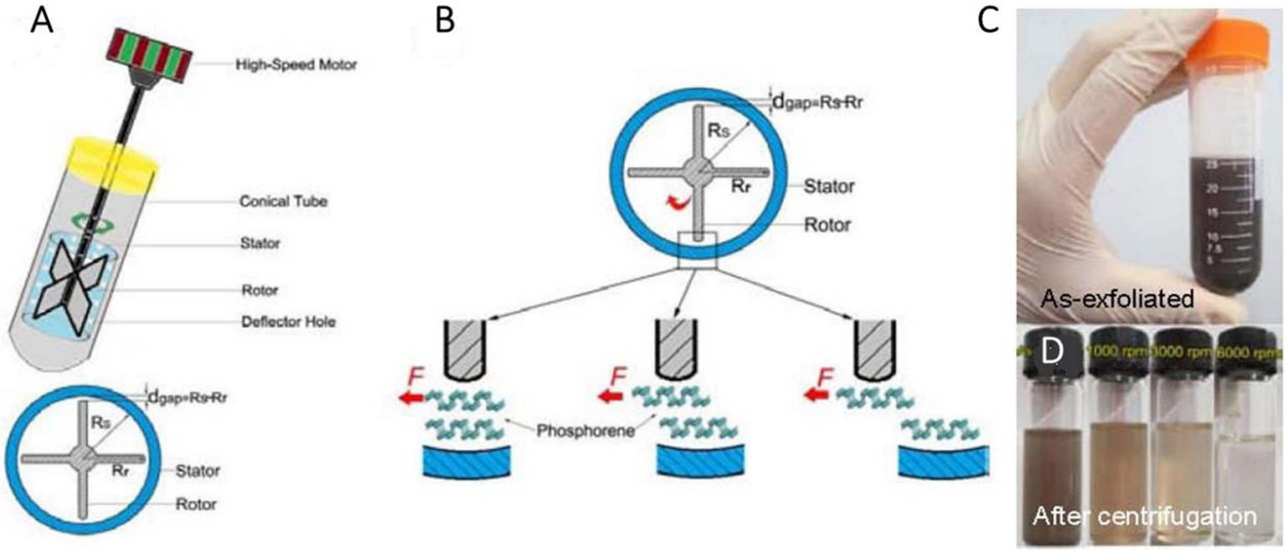

Fig. 5. Schematic illustration of (A) shear exfoliation setup and (B) shear exfoliation process. Photograph of as-exfoliated BP nanoflakes dispersed in NMP (C) before and (D) after centrifugation [63]. Copyright © 2015 WILEY-VCH Verlag GmbH & Co. KGaA, Weinheim.

overcome the energy barrier. Compared the graphene with highly exfoliated BP in the tested solvents, there exist a local minimum energy when there is only a thin "layer" of solvent embedded between the sheets by expelling the most solvent molecules. Finally, there is no lateral movement and a meta-stable lattice-like plane with limited vibrations can be formed by these residual solvent molecules, hence result in stable BP-solvent interactions. On the other hand, BP flakes can be exfoliated and dispersed in target solvents through tuning the energy of this thin solvent "layer", and open a lower energy path towards aggregation. Of course, solvents selected as efficient exfoliation media should be still kept balance between the ease of exfoliation and difficulty of suspension, so as to induce a satisfied BP suspension yield.

It should be noted here that BP is unstable in pure water or air due to the photo-oxidation at the BP surface induced by oxygen and light [60]. As shown in Fig. 6A, there exist bubbles on the sur-

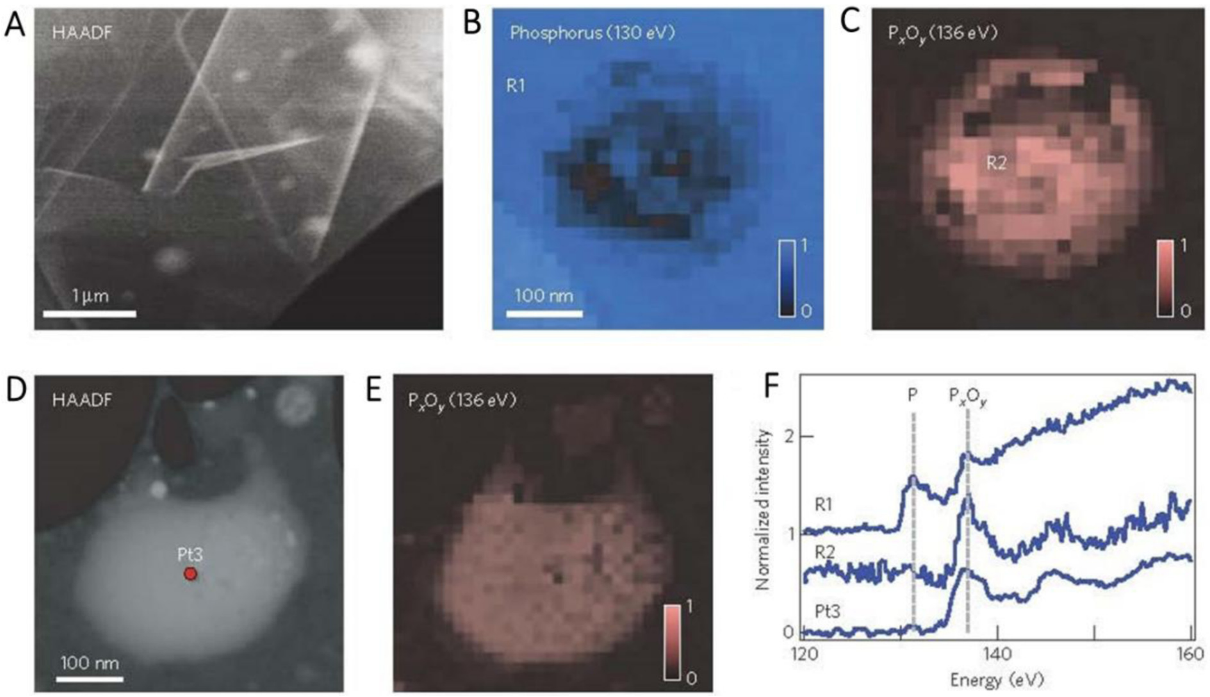

Fig. 6. High-angle annular dark-field (HAADF) contrast images and core-loss images of oxidized BP recorded at 80 kV. (A) HAADF contrast image of a flake (20 layers) after 1 h light exposure in air. Extracted chemical maps on a bubble based on multiple least squares analysis of the reference spectra of (B) P-pristine at 130 eV and (C) P_xO_y at 136 eV. (D) HAADF and (E) core-loss images of the P_xO_y feature at 136 eV. (F) EELS spectra extracted from regions R1 and R2 in (B) and (C) compared against the TEM-EELS spectrum in position Pt3 of (D) [65]. Copyright © 2015, Rights Managed by Nature Publishing Group.

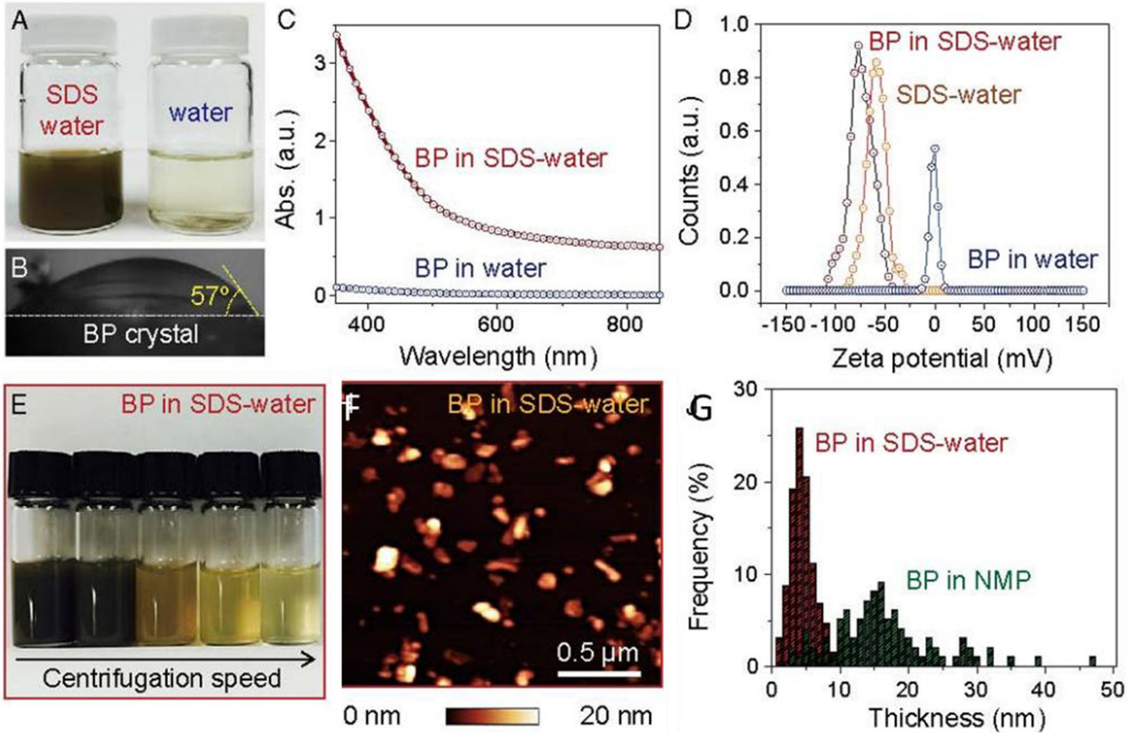

Fig. 7. Surface properties and exfoliation yield of BP in aqueous solution. (A) Photograph of a BP dispersion in deoxygenated water with and without SDS. (B) A water contact angle measurement performed on the surface of an as-exfoliated flat BP crystal. (C) Optical absorbance spectra of BP dispersions with (red) and without (blue) SDS. (D) Zeta potential measurement of BP in water (blue), SDS water (orange), and BP in SDS water (red). (E) Photograph of BP dispersions in SDS water after sonication and centrifugation. (F) AFM height images of BP flakes processed in SDS-water. (G) Thickness distribution of BP flakes in SDS-water (red) and NMP (green) [58]. Copyright © 2016, National Academy of Sciences.

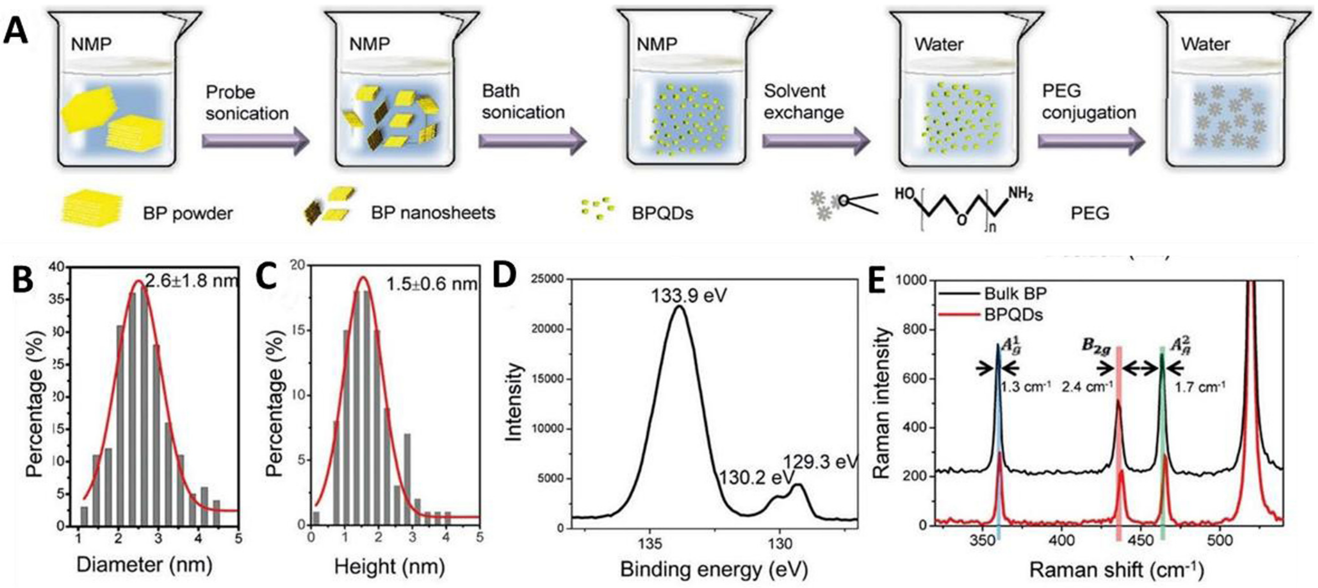

Fig. 8. Synthesis process and characterizations of the BPQDs. (A) Synthesis process of BPQDs. (B) Statistical analysis of the lateral sizes of BPQDs determined by TEM. (C) Statistical analysis of the heights of BPQDs determined by AFM. (D) XPS spectrum and (E) Raman spectra of the as-prepared BPQDs [70]. Copyright © 2015 WILEY-VCH Verlag GmbH & Co. KGaA, Weinheim.

Fig. 9. Schematic illustration of the disintegration process from bulk BP crystal to BPQDs using a household kitchen blender [71]. Copyright © 2016 WILEY-VCH Verlag GmbH & Co. KGaA, Weinheim.

face of BP after exposing in air for 1 h. Fig. 6B and C reveals a typical bubble composed of oxidized P atoms surrounded by pristine P. After many days in ambient conditions with light irradiation, the sample is completely oxidized (Fig. 6D–F) and a possible light-induced oxidation mechanism for BP can be expressed as follows [65]:

$$\theta + h\nu \leftrightarrow \theta^* \tag{1}$$

$$\theta^* + O_{2(aq)}^{\cdot-} + \theta + h^+ \rightarrow \theta_{ox} \tag{2}$$

In Eq. (1), a photo excitation produces excitons, whose steady-state population, θ^*, depends on the photon flux, absorption cross-section and recombination rate. Here, θ presents a light-induced oxidation mechanism of 2D-phosphorus of coverage. In Eq. (2), the photo-induced excitons produce the charge carriers for transfer reaction towards aqueous oxygen molecules at the surface. This reaction hole (h^+) dopes BP and generates reactive intermediate superoxide anions, $O_{2(aq)}^{\cdot-}$, that react spontaneously with p-doped BP to form oxides of coverage θ_{ox}. Therefore, it is necessary to avoid oxygen when using water or water related solvents to exfoliate BP flakes. An effective way to stably disperse BP in water is to purge deionized water with ultrahigh-purity Ar gas in a sealed container [54,58,66] and high yield ultrathin BP flakes can be achieved in SDS (sodium dodecyl sulfate)-water as shown in Fig. 7 [58]. It reveals the effectiveness of aqueous surfactant solutions for the preparation of ultrathin BP flakes as compared to organic solvents, which also implies the BP exfoliation yield monotonically increases with the increase of surface tension. An average contact angle of ~57° measured on BP surface can be obtained, indicating its moderate hydrophilicity which is between graphene oxide (~27°) and other 2D nanomaterials (~90°) [67,68]. Another methodology to prevent the degradation of BP is to choose suitable solutions beyond water, as the solutions we mentioned above. The details of solvation shell in selected solutions (such as CHP) for protecting the nanosheets from reacting with oxygen or water had been proved by Hanlon et al. [56].

BP quantum dots

It is well known that some improved or new properties will arise when 2D materials transformed to 0D forms (i.e. lateral sizes being reduced to typically < 20 nm) followed by the prominent edge and quantum confinement effects. Compared with their native 2D forms, such new class of 0D materials (quantum dots) display larger surface-to-volume ratio, better solubility in both aqueous and non-aqueous solvents, higher tunability in physiochemical properties, better amenability to hybridize with other nanomaterials, and more easy to be doped and functionalized. For example, graphene quantum dots (GQDs), derived from graphene sheet, exhibit widely tunable photoluminescence properties and ultra-broadband optical absorbance when compared to its 2D counterparts. Therefore, it is of great importance to explore the synthesis method and applications of black phosphorus quantum

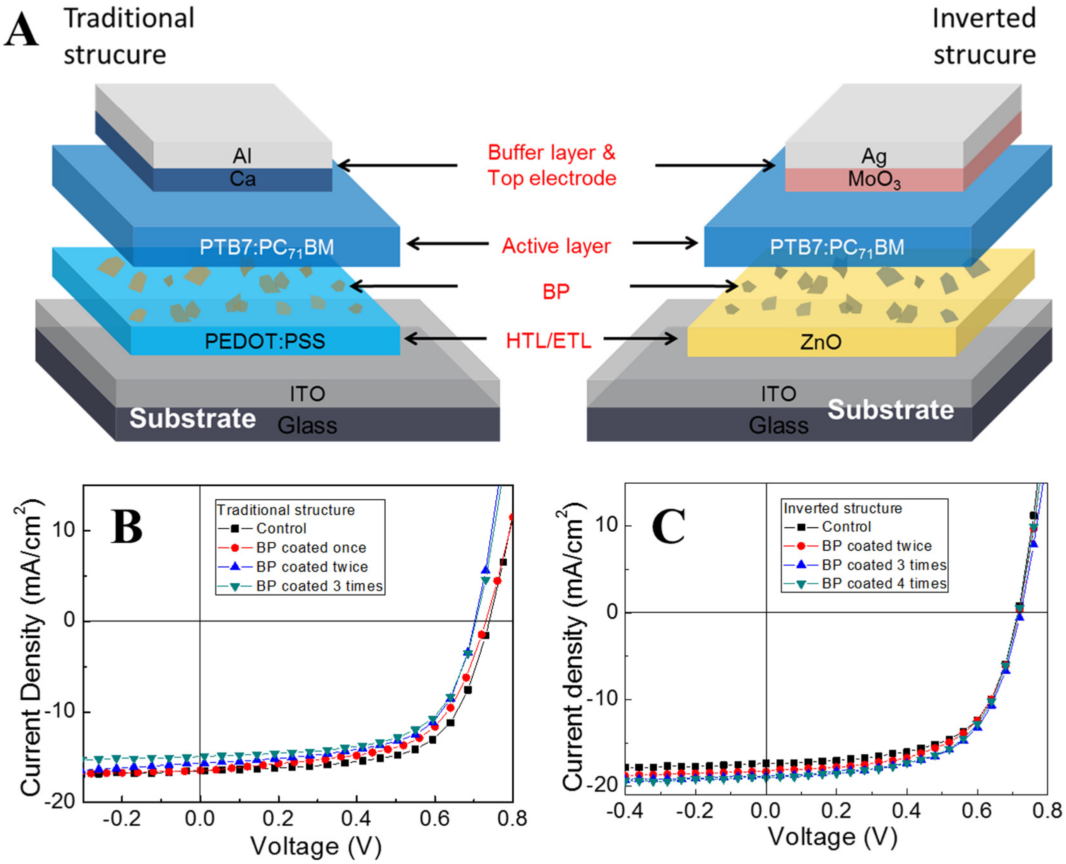

Fig. 10. (A) Conventional and inverted architectures of OPVs based on PTB7:PC$_{71}$BM; J–V characteristics of (B) conventional, and (C) inverted OPVs with BP incorporation under different conditions [11]. Copyright © 2016 WILEY-VCH Verlag GmbH & Co. KGaA, Weinheim.

dots (BPQDs). Interestingly, it is reported that BPQDs can be prepared through direct ultrasonication [69,70], or high turbulent shear rate generated from a household kitchen blender [71], which adds a new dimension to BP research and extend the applications of 2D nanosheets to 0D quantum dots.

As shown in Fig. 8, BPQDs derived from bulk BP crystal could be realized by combining probe sonication with bath sonication, which obviously improves the sonication efficiency when compared to the synthesis process by grinding followed by ice-bath sonication of micrometer-sized BP crystals [66]. The average lateral size of the as-obtained BPQDs was 2.6 ± 1.8 nm and the corresponding average thickness was 1.5 ± 0.6 nm, which were smaller and thinner than that of the sample prepared by grinding followed by sonication. X-ray photoelectron spectroscopy (XPS) of the BPQDs revealed the feature peaks of crystalline BP located at 129.3 eV ($2p^{3/2}$) and 130.2 eV ($2p^{1/2}$) [54]. The oxidized phosphorus (i.e. PO_x) at 133.9 eV [54] can also be observed due to its easy oxidation in water under visible-light irradiation. Based on the Raman spectra, the A_g^1, B_{2g}, and A_g^2 modes of the BPQDs exhibited red-shifted when compared to that of bulk BP [21]. On the other hand, an ultrafast and more efficient method by using a household kitchen blender, was put forward to prepare BPQDs (see Fig. 9). BP sheets were firstly obtained through shear exfoliation and then gradually converted into BPQDs via a layer-by-layer disintegration process [71]. A possible formation mechanism of BPQDs by household kitchen blender was also proposed. The Reynolds number (Re_{Blade}) associated with the blender is expressed as follows:

$$Re_{Blade} = ND^2\rho/\eta \tag{3}$$

where N is the rotor speed, D is the rotor diameter, ρ and η are the liquid density and viscosity respectively. By comparing and estimating the size of BPQDs and the mean turbulent shear rate, the feasibility of disintegrating BP into BPQDs by the kitchen blender can be determined. Ultrasmall size BPQDs (∼2.2 ± 0.4 nm) can be obtained through turbulent disintegration method within ultrashort time (only ∼ 0.66 h) [71], which paves a simple and highly efficient way to the scalable production of BPQDs. It should be noted here that the separation of BP nanosheets from the solvent is one of important factors for the successful preparation of solution-exfoliated BP. The key is the centrifuging speed, for example, BP flakes could be obtained from the suspension at a low centrifuging speed (∼higher than 1000 run/min) [11], while BPQDs could only be obtained at a higher centrifuging speed (∼higher than 7000 run/min) [69,70].

Generally, BP flakes or BPQDs can be easily fabricated through sonication-assisted solution process. Although liquid-exfoliation of BP can be kept stable in diverse solutions such as IPA, NMP and ethanol for a long time [11], a key challenge of BP nanosheets is still the surface degradation. Excluding the encapsulation of passivation layer onto BP surface for moderately repressing its surface degradation, surface functionalization engineering is also a good strategy for the enhancement of surface stability for BP. For example, Ryder et al. had reported that covalent aryl diazonium functionalization could suppress the chemical degradation of exfoliated BP with ambient exposure [72]. Yue et al. showed that the air-passivated ambipolar BP transistor formed by applying benzyl viologen is stable [73]. In this viewpoint, we can possibly tune the stability of BP flakes or BPQDs in solutions or air through

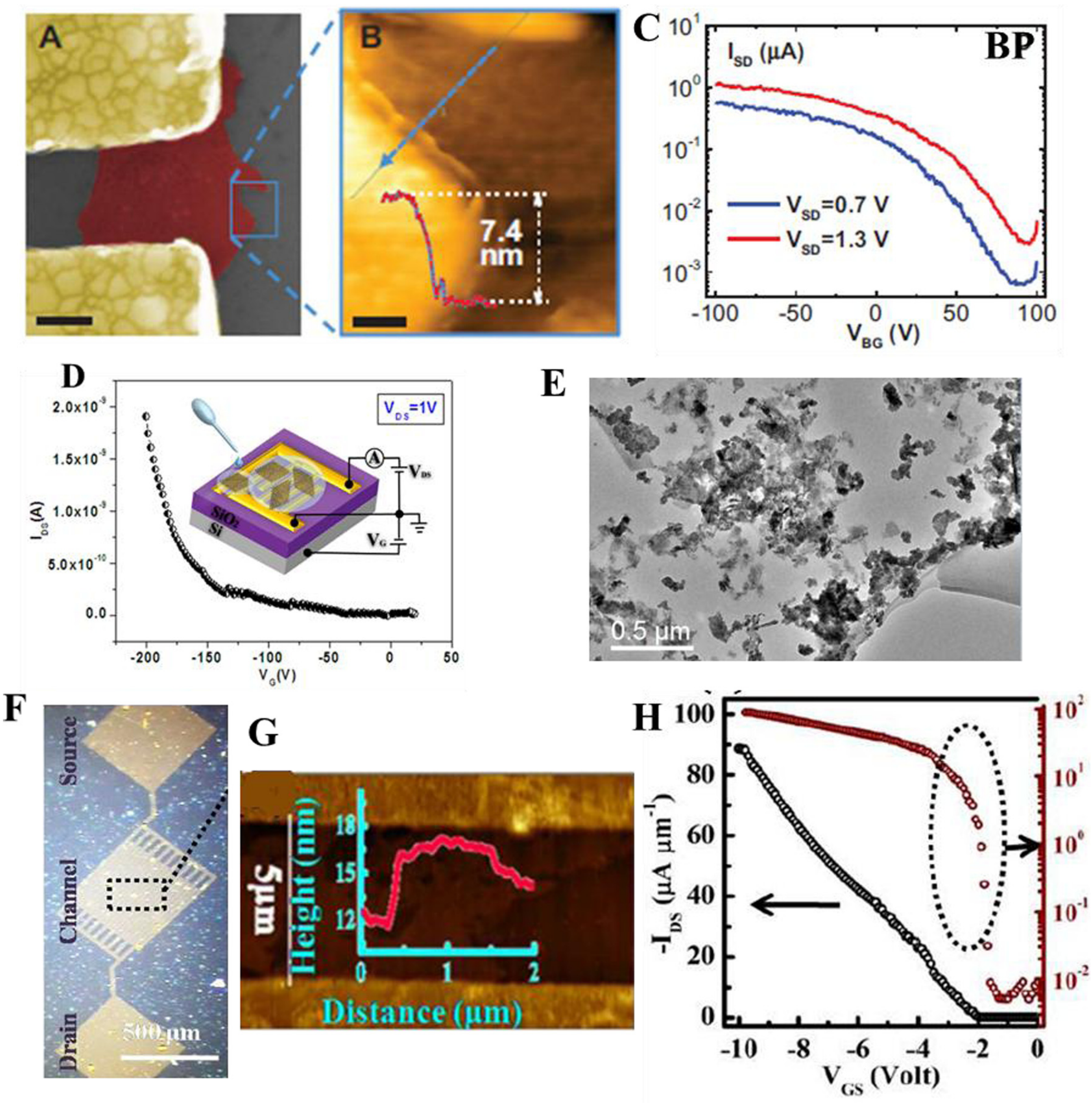

Fig. 11. Electrical characterization of (A–C) individual flake FETs and (D–H) drop-casted FETs. (A) SEM image of FET structure based on an individual BP sheet; (B) AFM image of selected region in (A); (C) Source-drain current (I_{SD}) with respect to the applied back gate voltage (V_{BG}) swept from −100 to +100 V; (D) A typical I-V curve of the FET fabricated by drop-casting BP solution onto gold contacts. (E) TEM image of BP flakes in IPA. (F) Optical image of FET with LB assembled BP as a channel material. (G) AFM of exfoliated BP. Inset shows the variation of height of BP. (H) Variation of drain current I_{DS} with gate voltage V_{GS} (left y-axis is the linear scale, and right y-axis is the logarithmic scale). (A)–(C) [78], Copyright © 2015 WILEY-VCH Verlag GmbH & Co. KGaA, Weinheim. (D) and (E) [11], Copyright © 2016 WILEY-VCH Verlag GmbH & Co. KGaA, Weinheim. (F)–(H) [79]. Copyright © 2016, Rights Managed by Nature Publishing Group.

covalent functionalization engineering, which might extend the applications of exfoliated-BP in many fields.

Applications

BP flakes

Transport layer

It is well known that the doping level can be controlled by the field effect in an atomically thin semiconductor, enabling the implementation of electrically tunable p-n junctions which is different from that induced by ionic dopants and extracted by the built-in electric field in conventional photovoltaic devices. It is exciting that BP possesses ambipolar transport property [74,75], which ensures the realization of p-n junction of BP by using h-BN as gate dielectric and BP as ambipolar semiconducting channel material, resulting in a strong photocurrent and a significant open-circuit photovoltage due to the photovoltaic effect [76], such that BP can be served as semiconductor for solar cell applications. We have successfully incorporated BP into organic photovoltaic structure as an effective electron transport layer, which leads to pronounced enhancement of the device performance [11]. As shown in Fig. 10, solution exfoliated BP flakes were spin-coated onto PEDOT:PSS and ZnO layers but not serve as a pure carrier-transport layer due to poor conductivity of the discontinuous separate BP film. By comparing the BP/PEDOT:PSS in conventional structure (as hole transport layer) and BP/ZnO in inverted structure (as electron transport layer), it was found that the BP flakes provided positive effect in inverted structure but negative effect in conventional structure. An average PCE (power conversion effi-

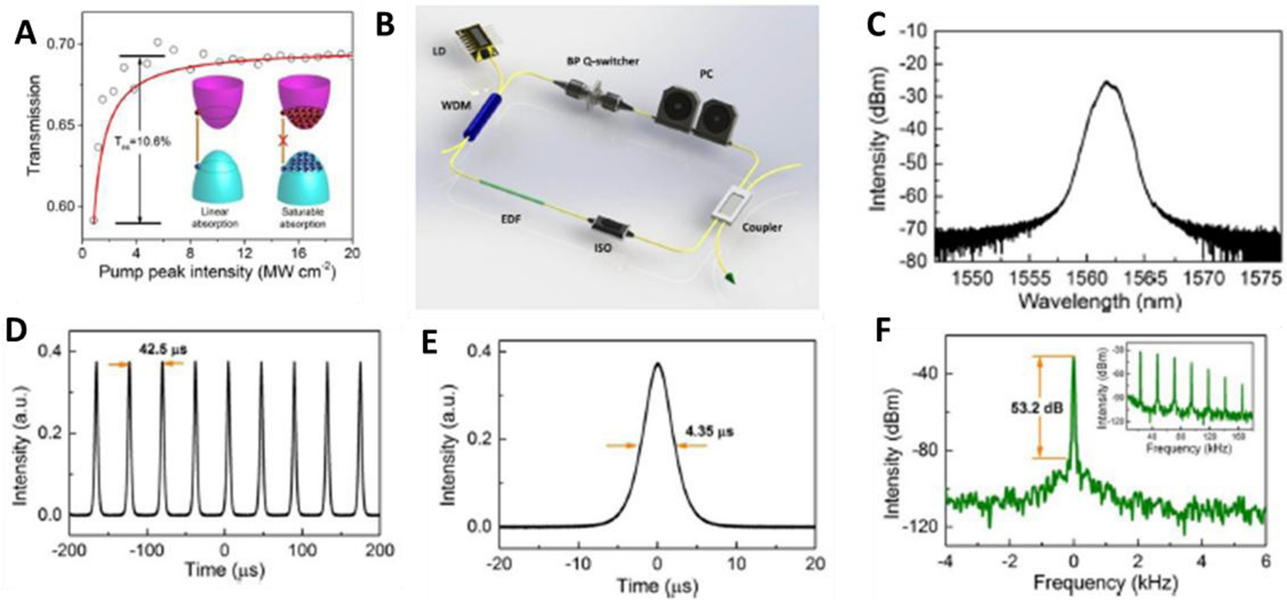

Fig. 12. (A) The collected saturable absorption curve of BP-polymer composites measured at 1565 nm. The insets show the energy diagrams of the saturable absorption and linear absorption. (B) Schematic illustration of the ring cavity of the utilized Q-switched fiber laser, where LD, ISO, WDM, PC and EDF respectively represent 974 nm laser diode, polarization-independent isolator, wavelength division multiplexer, polarization controller and erbium-doped fiber. (C) Optical spectrum of the Q-switching. (D) Q-switching pulse train of the Q-switching. (E) Single Q-switching pulse. (F) The obtained radiofrequency optical spectrum at the fundamental frequency and the wideband RF spectrum (inset) [55]. Copyright © 2015 WILEY-VCH Verlag GmbH & Co. KGaA, Weinheim.

ciency) of the organic photovoltaics in inverted structure was enhanced by 11% relatively from 7.37% to 8.18% when compared to that of the control device, owing to a cascaded band structure prohibiting carrier recombination near the cathode by the incorporation of BP as electron transport layer. In addition, the incorporation of BP into organic photovoltaics exhibited improved stability in air due to the encapsulation of the devices, opening an avenue in using BP for the potential applications of photovoltaics. Although the use of BP as charge transport layer in organic solar cell seem promising, the discontinuous liquid-exfoliated BP film would limit its applications for serving as individual active layer. Once BP flakes or BPQDs can be individual or incorporated with conducting polymer to form a continuous film, its application in active layer could be realized in the future.

Field effect transistors

Although mechanically exfoliated BP shows great applications in the field of field-effect transistors (FETs) [22], the fabrication of large-scale BP-based optoelectronic devices is still a challenge. On the contrary, liquid-phase exfoliated BP offers a possible way for solution-processed electronic and optoelectronic devices [31,77]. Therefore, it is necessary to discuss the fabrication and characterization of solution-processable BP-based FET, and hence giving a guidance for scalable production of BP-based optoelectronic devices.

Yasaei et al. [78] demonstrated that high-quality atomically thin BP flakes could be obtained by liquid-phase exfoliation in several solvents and the on/off ratio of BP-FET could be up to $\sim 10^3$ but with low carrier mobility of ≈ 0.58 cm^{2}V^{-1} s^{-1} (see Fig. 11A–C). It should be noted that such BP-FET is only fabricated on individual BP sheet (7.4 nm thick). After depleting the oxygen in the solutions by purging argon gas, the as-obtained BP flakes seemed more stable in the solutions [54]. The measurements of such BP-FETs showed typical ambipolar behavior with a median hole mobility of 25.9 cm^2 V^{-1} s^{-1} and an on/off ratio of 1.6×10^3, which significantly improved the mobility of FET fabricated on individual solution-processed BP sheet, but still limited to several micron scale. Indeed, large scale BP-FET can be realized. To do this, metal contacts (gold) was firstly deposited on SiO_2/Si substrate by standard photolithography process through a stencil mask aligned with the substrate. Then BP solution was drop-casted onto the gold contacts to form FET. However, this process requires highly continuous and uniform BP films formed by the restacking of BP flakes. If the drop-casted BP film is not continuous, the resulting mobility could be very low ($\sim$0.002 m^2/V S) even with an on/off ratio of $\sim$2000 (see Fig. 11D and E), which is much lower than that of mechanically exfoliated BP due to the longer channel width and inhomogeneous BP film. In contrast, high on/off ratio of 10^4 can be achieved through forming a continuous and uniform BP film prepared by Langmuir Blodgett (LB) method [78]. Compared Fig. 11E with Fig. 11G, it is obvious that the BP films formed by LB method are continuous, which ensures the large scale fabrication of BP-FET and reveals great potential in large area BP optoelectronics.

Optical devices

Followed by the preliminary applications of solution-processable BP flakes in the field of FETs, BP flakes were utilized in optical devices to show their unique nonlinear properties. It has been demonstrated that dispersion of few-layer BP exfoliated in CHP solution possesses impressive nonlinear optical properties, which allows its applications in optical switching devices [56]. Meanwhile, mechanically exfoliated BP flakes have been developed as an effective saturable absorber (SA) for the ultrafast laser photonics, demonstrating a modulation depth of 18.55% and saturation intensity of 10.74 MW/cm^2 by using BP with moderate thickness [80]. As compared to mechanically exfoliated BP, solution-processed BP flakes also exhibit similar nonlinear properties. In our previous work [55], solution-processed BP flakes were incorporated into polymer matrices (BP-PVP nanofibers fabricated by electrospinning), where the composite not only protect BP from photooxidation [64] but also increase its processability and compatibility to photonic components. The saturable absorption property of the

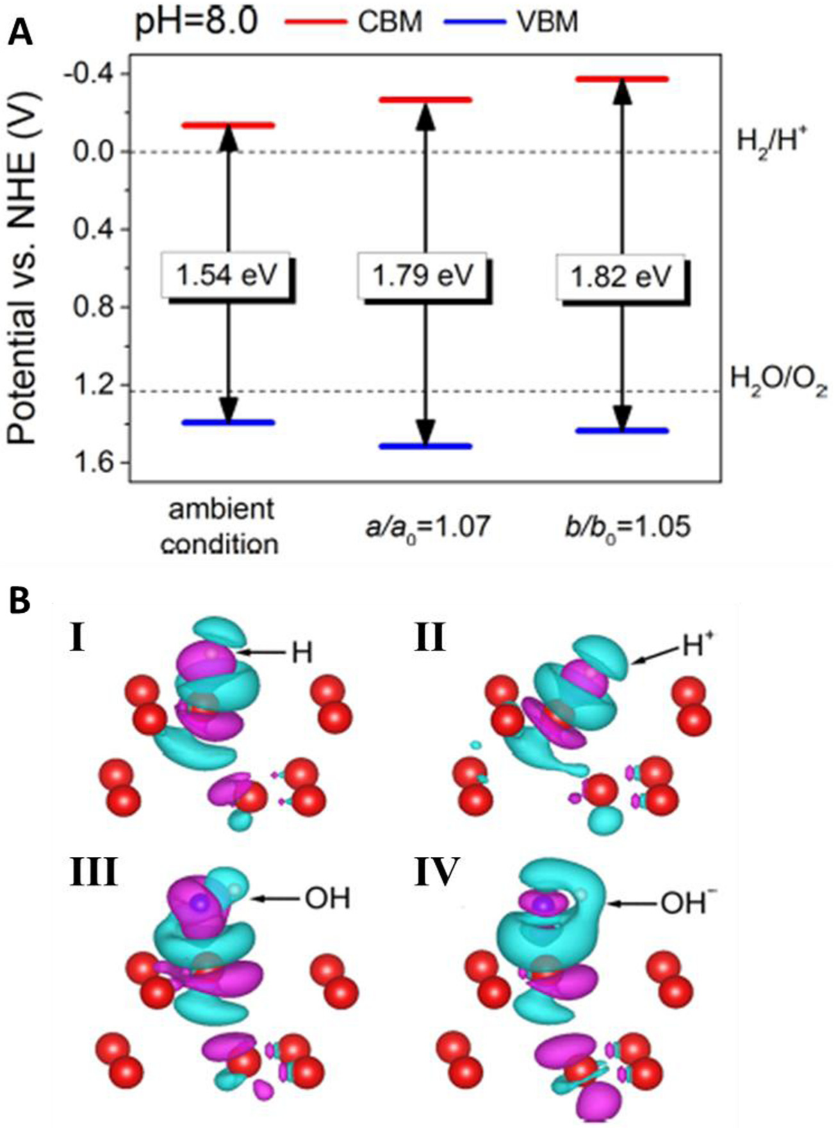

Fig. 13. (A) Energy alignment of BP under ambient conditions with 5% tensile strain along the *a* axis and 7% tensile strain along the *b* axis in a solution of pH = 8.0. The dashed lines are water redox potential in pH = 8.0 solution. (B) Plot of charge density difference (violet: charge depletion, cyan: charge accumulation) for (I) H, (II) H^+, (III) OH, and (IV) OH^- absorbed on top of BP [89]. Copyright © 2014, American Chemical Society.

BP-PVP composites measured at 1565 nm is displayed in Fig. 12A. Typically, the saturable absorption of BP can be expressed as [55]

$$\alpha(I) = \frac{\alpha_S}{1 + I/I_S} + \alpha_{NS} \quad (4)$$

where α_S and α_{NS} represent the saturable and nonsaturable absorption, respectively. I_S represents the saturation intensity, which is defined as the optical intensity required in a steady state to reduce the absorption to half of its unbleached value. By introducing BP-PVP into Q-switched fiber laser (Fig. 12), it showed a 3 dB bandwidth of 1.5 nm operated at a central wavelength of 1561.9 nm. Meanwhile, the generated pulse has a full width at half maximum (FWHM) of 4.35 μs with a symmetric intensity profile at a time interval of 42.5 μs. It also revealed a high performance output pulse with a signal-to-noise ratio of >53 dB and the modulation depth could be up to ~10.6%. Moreover, a single pulse energy of 194 nJ can be achieved. In addition to pulse laser, solution-processed BP also exhibited ultrafast recovery time of ~24 fs [81] when induced by intra-band relaxation process [82,83], which is much faster than that of previously reported 2D crystal materials. Obviously, solution-processed BP flakes play an important role as SA for pulse generation in fiber laser at telecom wavelength.

Photocatalyst

A photocatalyst is a kind of material that can stimulate the chemical reactions of a reagent by absorbing solar photons and transform the reagent into a final product without being consumed in the reaction [84,85]. Photocatalysis is really different from photochemical reactions. In a typical photochemical reaction, a photon absorptive substance acts as both a reagent and catalyst, and eventually being consumed during the reaction process to form the final product. In terms of photocatalysis, for example, photocatalytic water splitting decomposes water into hydrogen and oxygen with the aid of a semiconducting material that can absorb photons when irradiated by sunlight, but without consuming the semiconducting material. Generally, photo-catalytic water splitting process involves three main steps: (i) absorption of light to generate elec-

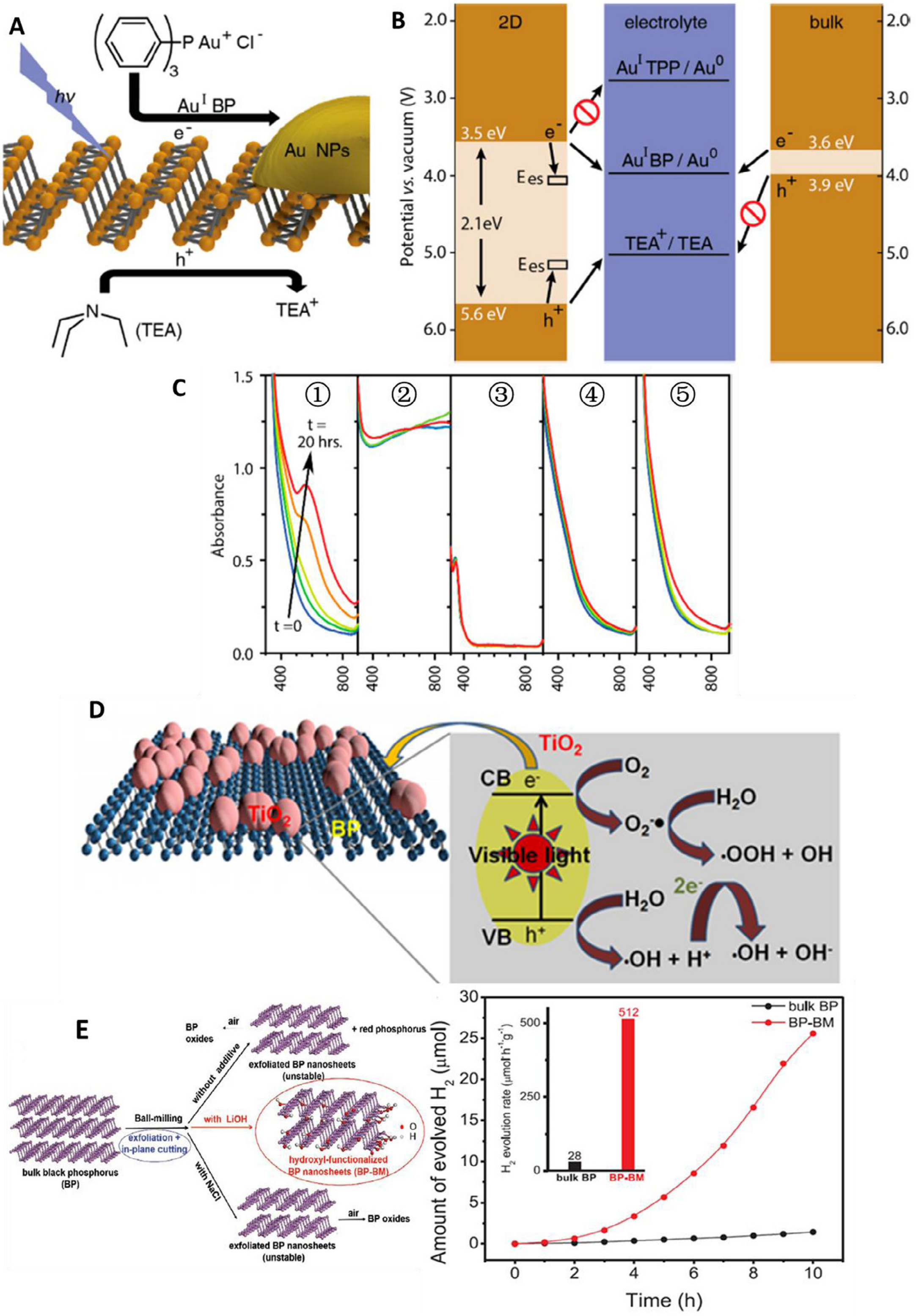

Fig. 14. (A) Light-driven redox reactions on 2D BP. Au^{I}TPP is converted to Au^{I}BP and reduced to Au nanoparticles (NPs), while trimethylamine (TEA) is oxidized to TEA$^+$. (B) An energy diagram shows the band edges of monolayer (2D) and bulk BP, redox potentials of each couple, and an indication of whether charge transfer is energetically favorable. The line accompanying Au^{I}TPP/Au^0 is not a formal reduction potential; rather, it marks the measured onset of an irreversible reduction of Au^{I}TPP to Au^0. E_{es} represents interband edge states, but the energy of these states is presently unknown. (C) UV−vis absorbance spectra of reactions that used standard conditions (TEA, Au^{I}TPP, light) with 2D BP (①), bulk BP (②), and without BP (③). Control experiments were also performed using 2D BP, Au^{I}TPP, but no TEA (④) and 2D BP, Au^{I}TPP, and TEA but with no light (⑤). (D) Proposed photocatalytic mechanism for BP@TiO$_2$ hybrid photocatalysts under visible light irradiation. (E) Left side revealed the ball-milling treatment of BP with or without additive. Right side showed the time courses of H$_2$ evolution from water using 5 mg bulk BP (black line) and 5 mg BP-BM (red line) photocatalysts dispersed in 100 mL aqueous solution containing 0.75 m Na$_2$S and 1.05 m Na$_2$SO$_3$ under visible light irradiation (λ > 420 nm). The inset shows H$_2$ evolution rates of bulk BP and BP-BM (BP ball-milled with additive). (A)–(C) are adapted from [90], Copyright © 2016, American Chemical Society. (D) is adapted from [91], Copyright © 2015, Rights Managed by Nature Publishing Group. (E) is adapted from [92], Copyright © 2017 WILEY-VCH Verlag GmbH & Co. KGaA, Weinheim.

tron–hole pairs; (ii) separation and migration of the photogenerated carriers to the surface of the photocatalyst; (iii) transportation of electrons and holes from the photocatalyst surface to the reactant molecules where H_2 or O_2 evolution taking place [86].

As a semiconducting material, BP possesses a direct bandgap ranging from 0.3 eV (bulk) to 2.0 eV (monolayer) which is broader than that of other 2D materials and most quantum dots, enabling BP to be an ideal photo-absorber to harvest solar energy [87]. Meanwhile, 2D semiconducting BP, similar to other 2D materials, may have several additional advantages over other nanomaterials in the following ways: (i) the surfaces of 2D materials intrinsically lack surface states, which is different from other materials [88], hence potentially afford longer carrier lifetimes and higher quantum yields; (ii) the loss related to carrier transport to the material's surface can be reduced due to the delocalized carriers in the 2D materials, which improves the feasibility of introducing carriers into the electrolyte, and (iii) the exciton binding energy (EBE) of 2D materials is extremely sensitive to the environment and can be favorably engineered to maximize the energy conversion efficiency. Especially for BP, the EBE can be lowered to ~15 meV through screening the excitons in a polar solvent [57], which maximizes the available energy for solar energy conversion as well as minimizing radiative recombination.

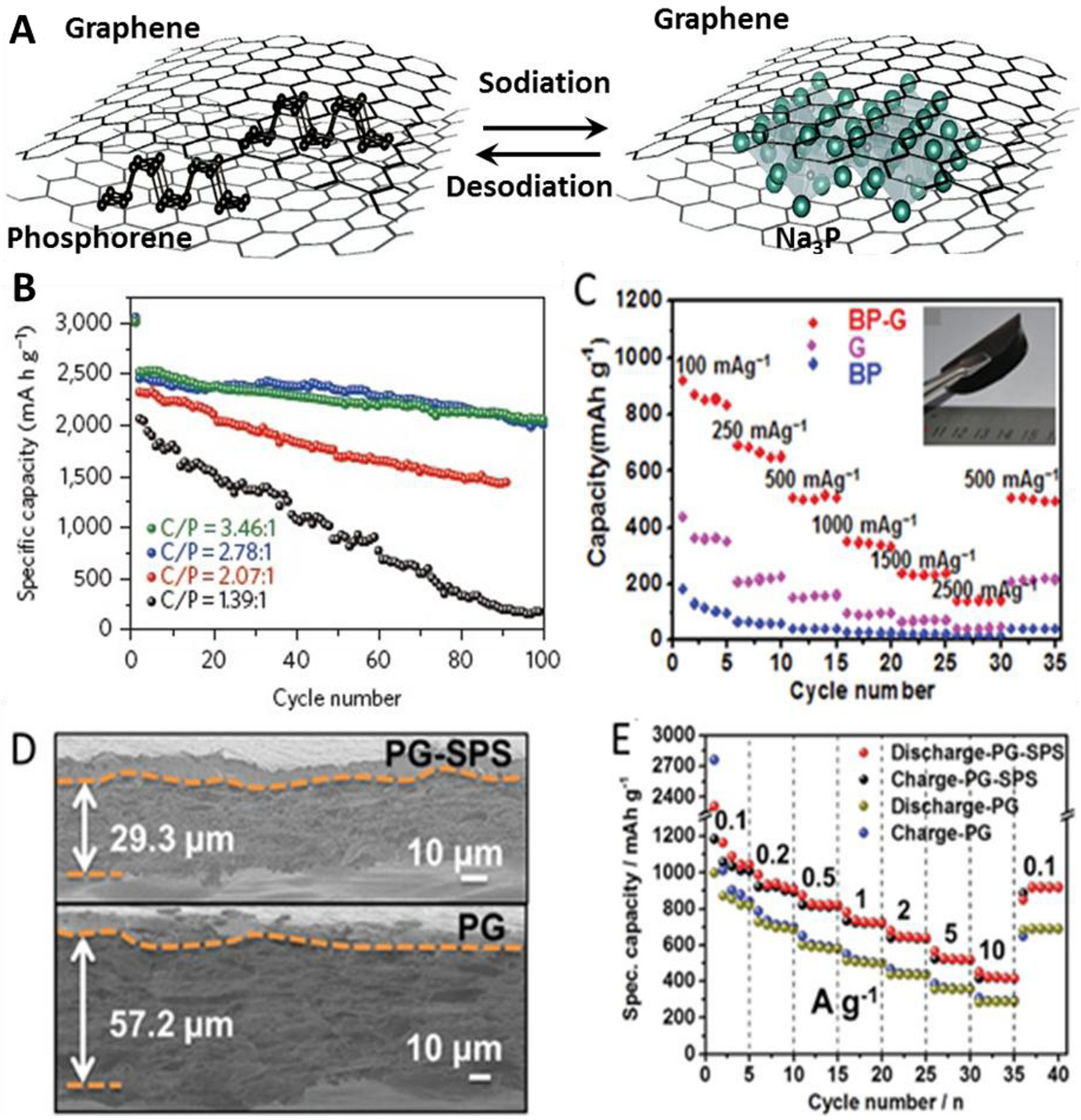

Fig. 15. (A) Schematic structural evolution of sandwiched BP-graphene during sodiation/desodiation [98]. (B) Reversible discharge capacity for the first 100 cycles of various BP-graphene samples with different carbon-phosphorus mole ratios (C/P) at current density of 50 mA h g^{-1} [98], Copyright © 2015, Rights Managed by Nature Publishing Group. (C) Rate performance of BP-G hybrid paper, BP nanosheets and graphene. Inset shows the photograph of the BP-G paper [100]. Copyright © 2016 WILEY-VCH Verlag GmbH & Co. KGaA, Weinheim. (D) Cross-sectional SEM images of PG-SPS and PG on Cu foil with the same loading mass [99]. Copyright © 2016 WILEY-VCH Verlag GmbH & Co. KGaA, Weinheim. (E) Rate performance of PG-SPS and PG electrodes [52]. Copyright © 2016 WILEY-VCH Verlag GmbH & Co. KGaA, Weinheim.

Interestingly, DFT (density functional theory) calculations [89] illustrate that the valence band maximum (VBM) of BP is more positive than that of the redox potential of O_2/H_2O, but the conduction band minimum (CBM) is more negative than that of the H^+/H_2 reduction potential, revealing BP has half influence on the water splitting. Meanwhile, the VBM and CBM of BP would be well suited to the redox potential of the water if the solution possesses a pH of 8.0 (see Fig. 13A), suggesting that BP could be suitable for solar water splitting. The potential water splitting capability of BP has also been studied through investigating the charge density difference. Simulation results (Fig. 13B) showed that the OH or OH^- absorption on one side of the BP can deplete the charges accumulated by absorption of H or H^+ on the other side, implying water reduction and oxidation might take place on different sides of the same BP.

In addition to the above-mentioned theoretical studies, the water splitting capability of BP was also experimentally investigated. Recently, Hu et al. [90] have demonstrated that BP became active for solar-to-chemical energy conversion when it was thinned down to 2D atomic layer by exploring its UV–vis absorbance properties. In their experiment, gold nanoparticles (NPs) were absorbed on the BP surface by the irreversible reduction of chloro (triphenylphosphine) gold (I) (Au^ITPP) and oxidation of triethylamine (TEA) (see Fig. 14A). Combining the prediction from the DFT calculations (Fig. 14B) with the experimental observations (Fig. 14C), it was concluded that the Au^ITPP reduction and TEA oxidation were exactly driven by splitting the photo-generated excitons of BP into electrons and holes, proving the feasibility of solar-to-chemical energy conversion by 2D BP. Apart from gold nanoparticles absorbed on BP surfaces, a hybrid of BP and TiO_2 can be also served as potential photocatalyst (Fig. 14D) for environmental and biomedical applications [91]. Compared to the high degradation rate of bare BP when exposed to visible light, BP hybridized with TiO_2 can reduce the degradation by 90%, due to the substitution of Ti atoms into the BP lattice that enhances the resistance of BP to moisture and oxygen. It is suggested that the stability of BP at ambient conditions should be improved to obtain an ideal photocatalyst through the hybridization of BP with other semiconductors or additives. Excitingly, it has been reported experimentally that the visible light photocatalytic hydrogen evolution rate of BP nanosheets can reach $512\ \mu mol\ h^{-1}\ g^{-1}$, which was ≈18 times higher than that of the bulk BP, and comparable or even higher than that of graphitic carbon nitrides ($g\text{-}C_3N_4$) [92]. Such breakthrough was realized by hydroxyl-functionalizing BP flakes with additional anhydrous lithium hydroxide (LiOH), which provides an insight into the utilization of functionalized BP for "metal-free" water splitting photocatalyst. In terms of a hybrid structure of BP with other 2D materials, it implies the thermodynamic bandgap requirement of a photocatalyst should be up to ∼1.23 eV for water splitting [85], i.e. the bandgap of hybrid BP/2D materials should be larger than 1.23 eV. For example, BP/WS_2 hybrid with a tunable bandgap of 0.89–1.44 eV [93] could be suitable for water splitting. However, sulfide compounds are also not stably prolonged and degraded in water when they are illuminated by light [94]. Thus, the chosen 2D materials, in a hybrid structure of BP/other 2D materials, should be also stable in water to protect BP either. In principle, BP/graphene hybrid structure, with a bandgap of ∼1.51–1.64 eV [95] tuned by the interaction between graphene and BP, might be suitable for water splitting.

Apart from the application of photocatalytic water splitting, Wang et al. [66] successfully demonstrated that liquid-phase exfoliated BP flakes can be served as effective photosensitizers for the

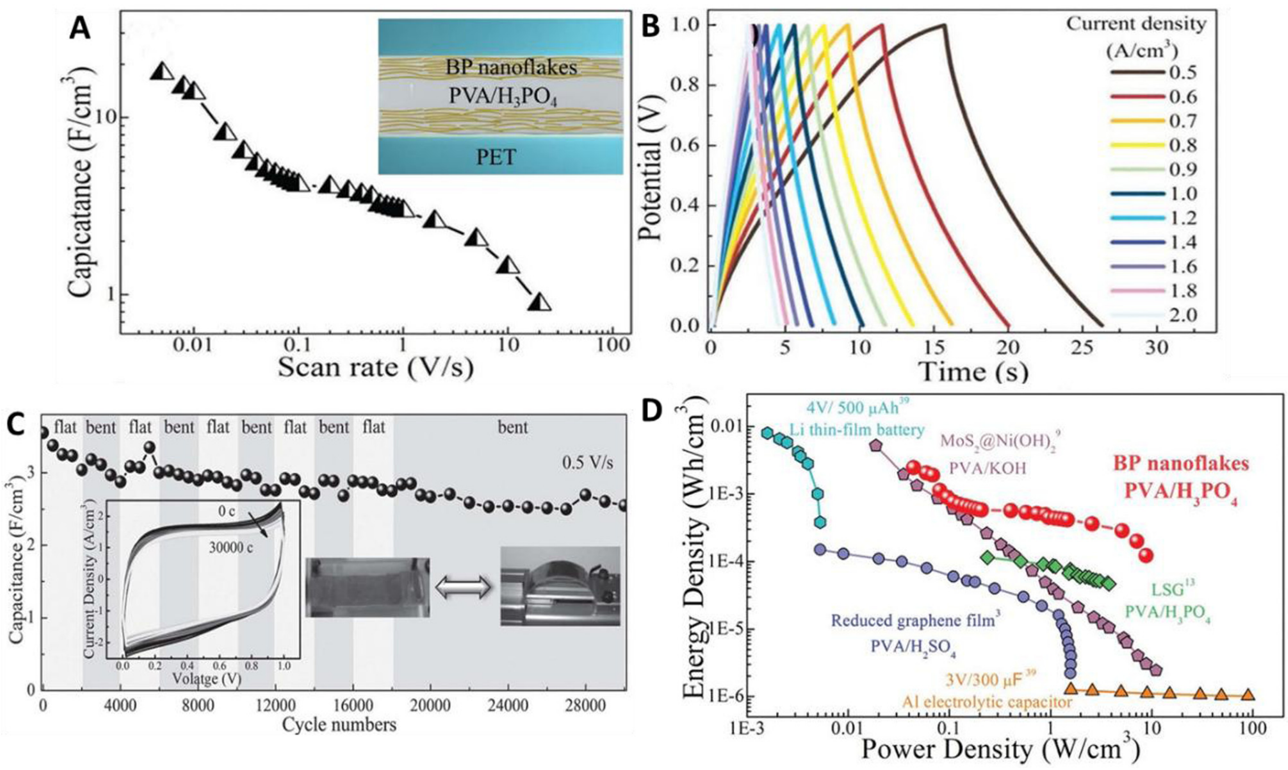

Fig. 16. (A) Capacitance of the BP-ASSP at different scan rates. Inset shows the schematic cross-section of the BP-ASSP. (B) Galvanostatic charge/discharge curves of the BP-ASSP at different current densities. (C) Cycling stability of the BP-ASSP at $0.5\ V\ s^{-1}$ under alternate flat and bent configurations. (D) Ragone plot of BP-ASSP and the performance comparison with several commercial energy-storage systems and reported devices [101]. Copyright © 2016 WILEY-VCH Verlag GmbH & Co. KGaA, Weinheim.

generation of singlet oxygen with a high quantum yield of about 0.91. As compared to bulk BP, such solution-processed BP flakes possess much more active sites for surface atoms, with reduced electron-hole recombination rate and faster charge carrier mobility, which promise attractive applications in catalytic and photodynamic therapy. It should be noted that the degradation of BP under prolonged exposure to light is still a serious problem needed to be resolved before the implementation of BP as an effective photocatalyst. In addition, Tao et al. [96] also demonstrated the potential of using BP flakes based nanomaterials as a robust delivery platform for cancer theranostics, which further enriches the utilizations of liquid-exfoliated BP flakes.

Energy storage devices

Energy storage devices such as Li-ion batteries and supercapacitors have been attracting great research attention since the rapid

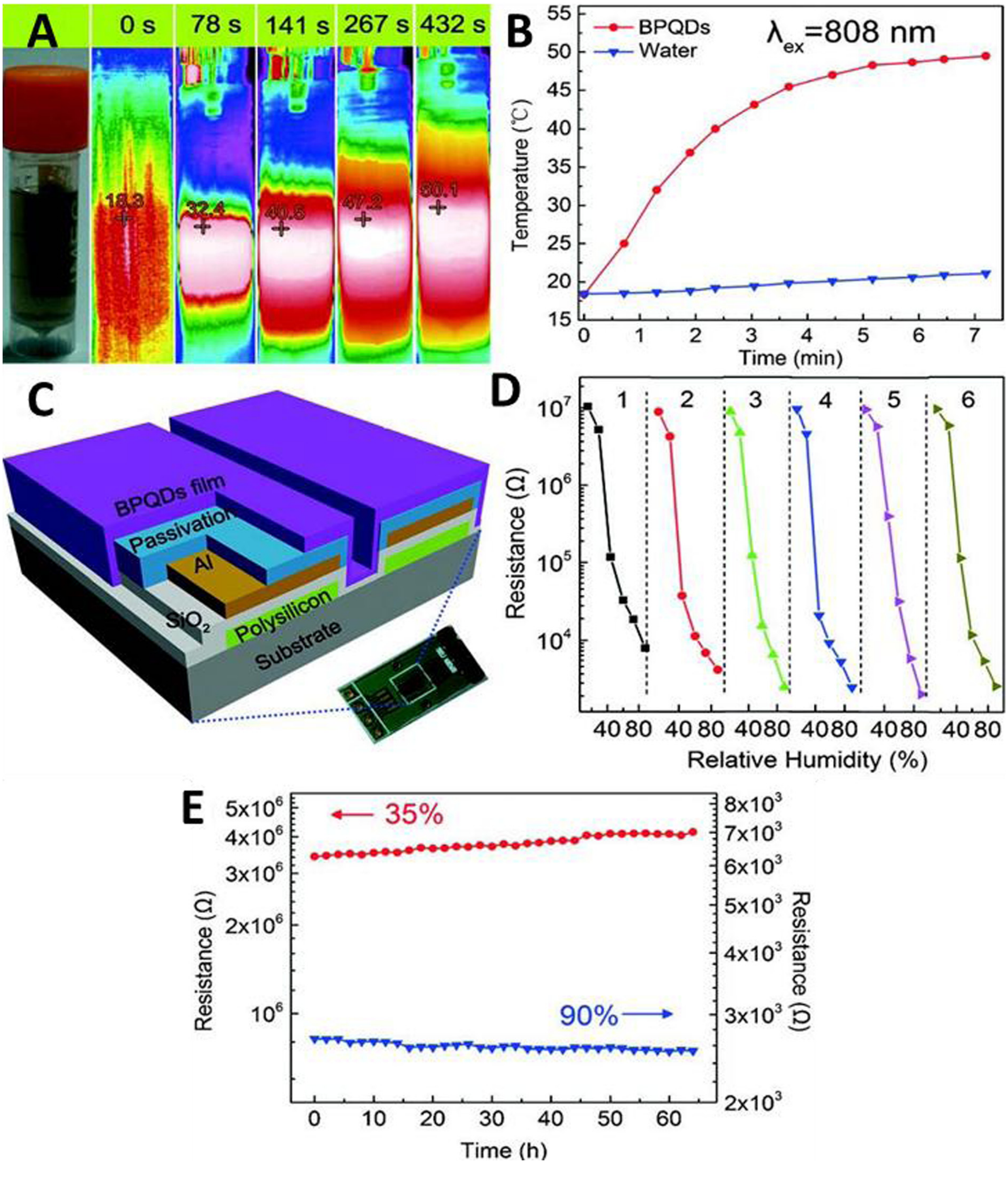

Fig. 17. (A) NIR thermal images of BPQDs solutions under different irradiation time with an 808 nm laser (1.5 W cm^{-2}). (B) The photothermal heating curves of pure water and BPQDs dispersed in water with certain concentration of 40 ppm. (C) Configuration of the interdigital resistive humidity sensor with BPQDs film as sensing material. Right inset is the optical photo of humidity sensor. (D) The sensing resistance with respect to relative humidity (RH) of sensor after six tests. (E) The stability of the humidity sensor in prolonged exposure to 35% and 90% RH at 21 °C [71]. Copyright © 2016 WILEY-VCH Verlag GmbH & Co. KGaA, Weinheim.

growth of portable electronics and the emerging development of electrical vehicles that demand for high performance mobile energy storage/supplying units. With a high theoretical specific capacity of 2596 mA h g^{-1}, BP has shown promising as Li-ion and Na-ion battery anode material. Particularly for Na-ion storage, BP possesses the highest theoretical specific capacity among all known materials. Nevertheless, BP suffers from huge volume change (about 300% [97] and 500% [98] for Li-ion and Na-ion storage, respectively) upon discharge and charge process, and eventually causes pulverization of the electrode material. To circumvent this problem, controlling the degree of Li-P reaction through limiting the discharge potential [99] or forming P-C chemical bonds [97] were reported to have significant electrochemical improvements. On the other hand, by minimizing the thickness of BP, it is expected the stress built up can be reduced when reacting with Li-ions or Na-ions [98]. Sun et al. prepared few-layered BP (1–5 layers) with enlarged interlayer distance by liquid-phase exfoliation [95]. The reaction mechanism of Na-P was evaluated by *in-situ* TEM and *ex-situ* XRD (X-ray diffraction) techniques, which involved the intercalation of Na-ions between BP layers followed by the formation of a Na_3P alloy, whereas the capacity was mainly attributed to the alloying process [98]. By mixing the as-prepared BP with graphene and subsequent solvent evaporation process, BP-G hybrid was formed with the BP layers sandwiched between graphene layers. Fig. 15A shows the schematic structural evolution of the sandwiched BP-G structure during sodiation and desodiation. The graphene acted as elastic buffer layers to accommodate volume change of BP during Na-ion uptake process and served as electrical highway for the electrode, while BP with enlarged interlayer distance offered short and effective path for Na-ion diffusion [98]. When evaluated as Na-ion battery anode, the BP-G hybrid showed a high specific capacity of 2440 mA h g^{-1} (based on the mass of BP only) at a current density of 50 mA g^{-1} and a capacity retention of 83% after 100 cycles. The cycling performance of various BP-G samples with different carbon-phosphorus mole ratios (C/P) is shown in Fig. 15B, which indicates the importance of graphene in stabilizing the electrochemical performance of BP-G anode.

In order to maximize the energy density of BP-G anode, Chen et al. fabricated flexible BP-G hybrid papers by vacuum filtration of a dispersion containing few-layered BP and graphene, and the hybrid papers were used directly as Li-ion anodes without the involvement of electrochemically inactive metallic current collec-

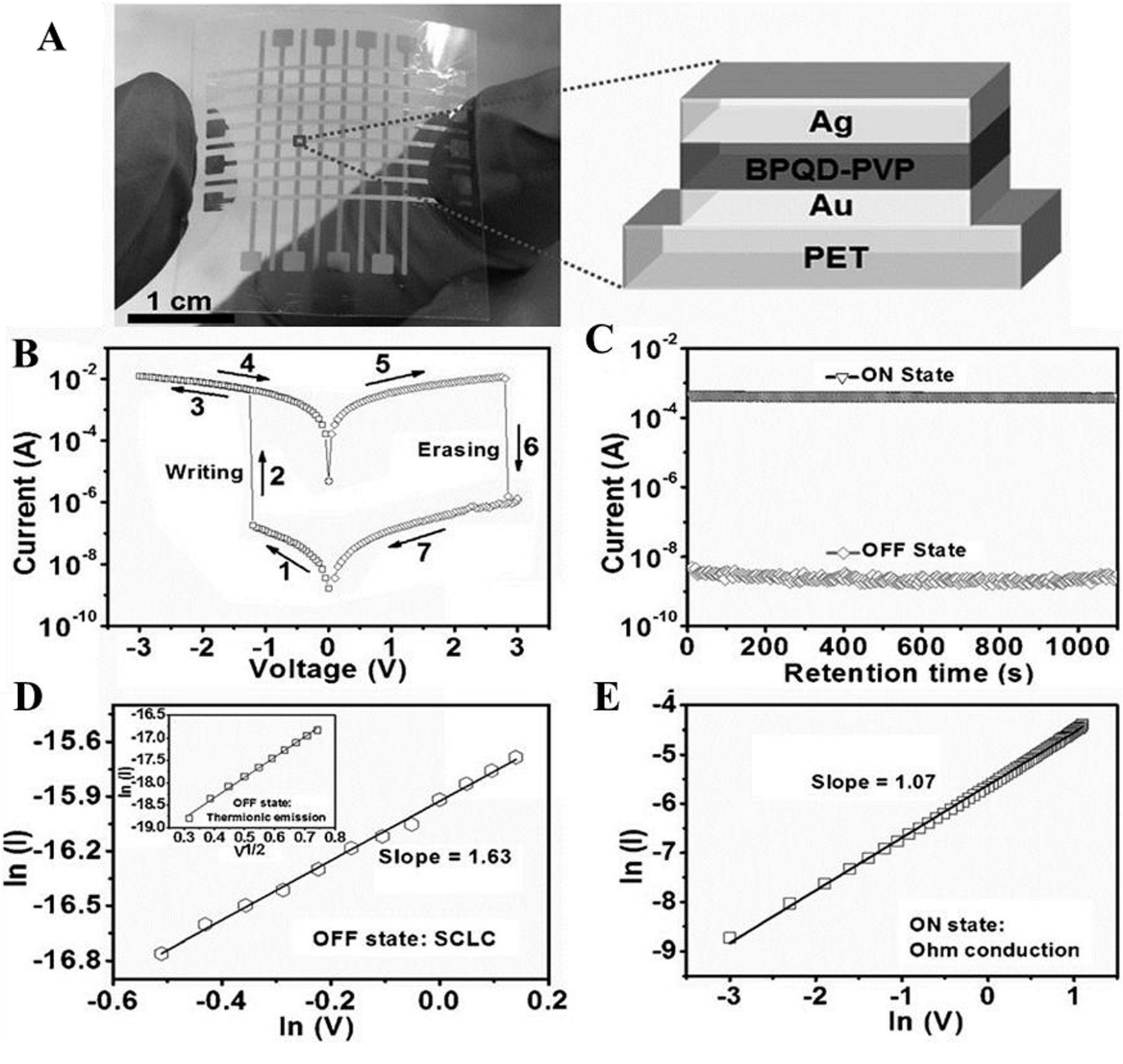

Fig. 18. Representation and characterization of the BPQD-based memory device [69]. Copyright © 2015 WILEY-VCH Verlag GmbH & Co. KGaA, Weinheim. (A) Photograph and illustration of the fabricated flexible memory device. (B) I–V characteristics of BPQD-based flexible memory device. (C) The retention-ability test of BPQD-based memory device in the ON and OFF states at reading voltage of 0.2 V. Experimental data and fitted lines of the I–V characteristics in the OFF state (D) and ON state (E).

tor, conductive additives and binders [100]. The BP-G paper delivered high specific capacity of 920 mA h g^{-1} at a current density of 100 mA g^{-1} and demonstrated prolonged cycling performance with specific capacity of 501 mA h g^{-1} at a current density of 500 mA h g^{-1}, based on the total mass of the electrode. Meanwhile, the BP-G paper exhibited superior rate performance (as shown in Fig. 15C).

Though significant electrochemical enhancement has been achieved by incorporating graphene with BP, the practical implementation of BP-based battery is still limited by the production yield of BP. Zhang et al. compared the yield of BP in different solvents by liquid-phase exfoliation and showed that the highest yield (38%) can be obtained by using formamide among all tested solvents [99]. The effect of packing density of BP-G on battery performance was also investigated. The as-prepared BP was mixed with graphene oxide (GO) and the mixture was vacuum filtrated to form PGO (porous graphene oxide) paper. The PGO was then reduced by spark plasma sintering (SPS) process to form PG-SPS, or by conventional sintering method to form PG (The cross-sectional SEM images of PG-SPS and PG are shown in Fig. 15D). The densely-stacked PG-SPS was demonstrated to be highly stable upon ambient exposure, due to the high packing density effectively prevented the access of oxygen and water to BP [52]. When used as Li-ion battery anode, the densely-stacked PG-SPS showed significant improvement on the initial Coulombic efficiency (60.2% compared to 34.3% of loosely-stacked PG), specific capacity and rate capability (Fig. 15E), which can be ascribed to the intimate contact between BP and G that reduced the side reactions with electrolyte due to lower exposed specific surface area, as well as fast electron kinetics in the densely-packed regime [52].

As a 2D material with large specific surface area, BP is suitable as electrode material of electrical double-layer capacitor (EDLC)

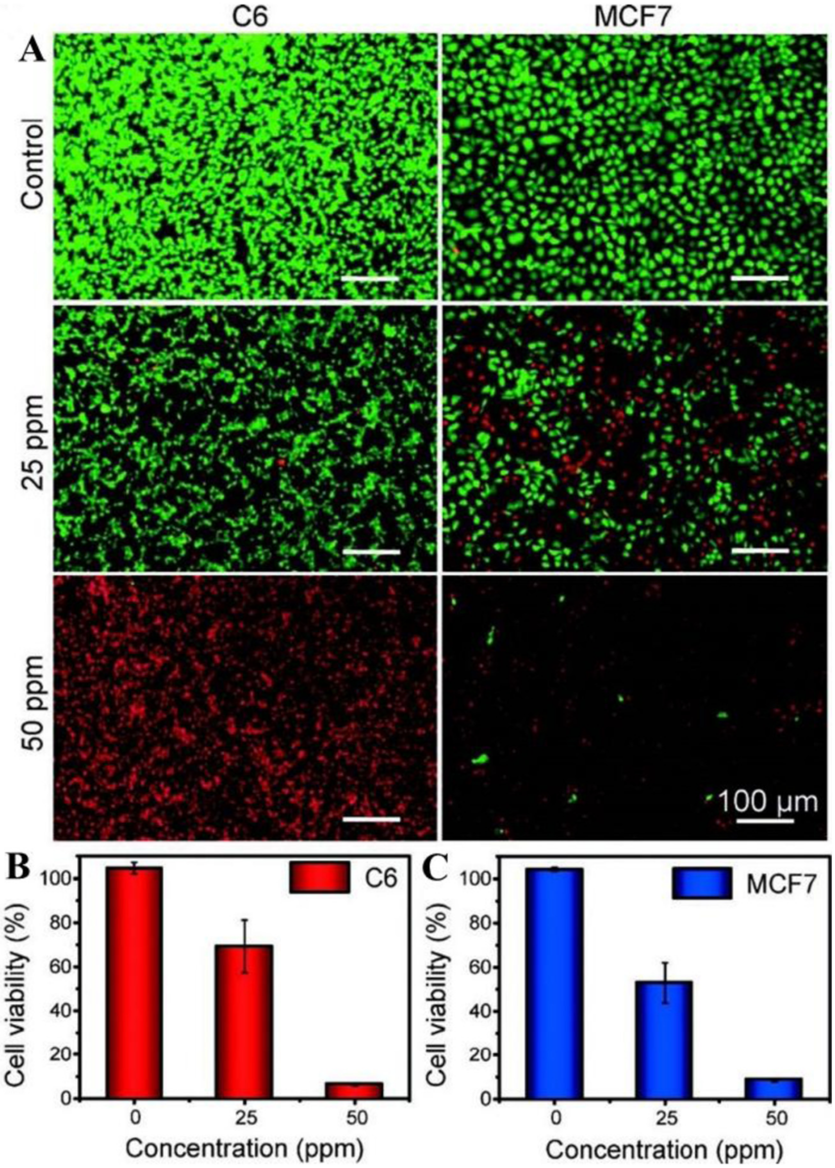

Fig. 19. Comparison of the photothermal destruction of C6 and MCF7 cancer cells upon addition of BPQDs (0, 25, or 50 ppm) and irradiation with an 808 nm laser at 1.0 W cm^{-2} for 10 min. (A) Fluorescence images of cells stained with calcein AM (live cells, green fluorescence) and PI (dead cells, red fluorescence). (B) Relative viabilities of C6 cells after the various treatments. (C) Relative viabilities of MCF7 cells after the various treatments. Error bars are based on the standard deviations (SDs) of six parallel samples [70]. Copyright © 2015 WILEY-VCH Verlag GmbH & Co. KGaA, Weinheim.

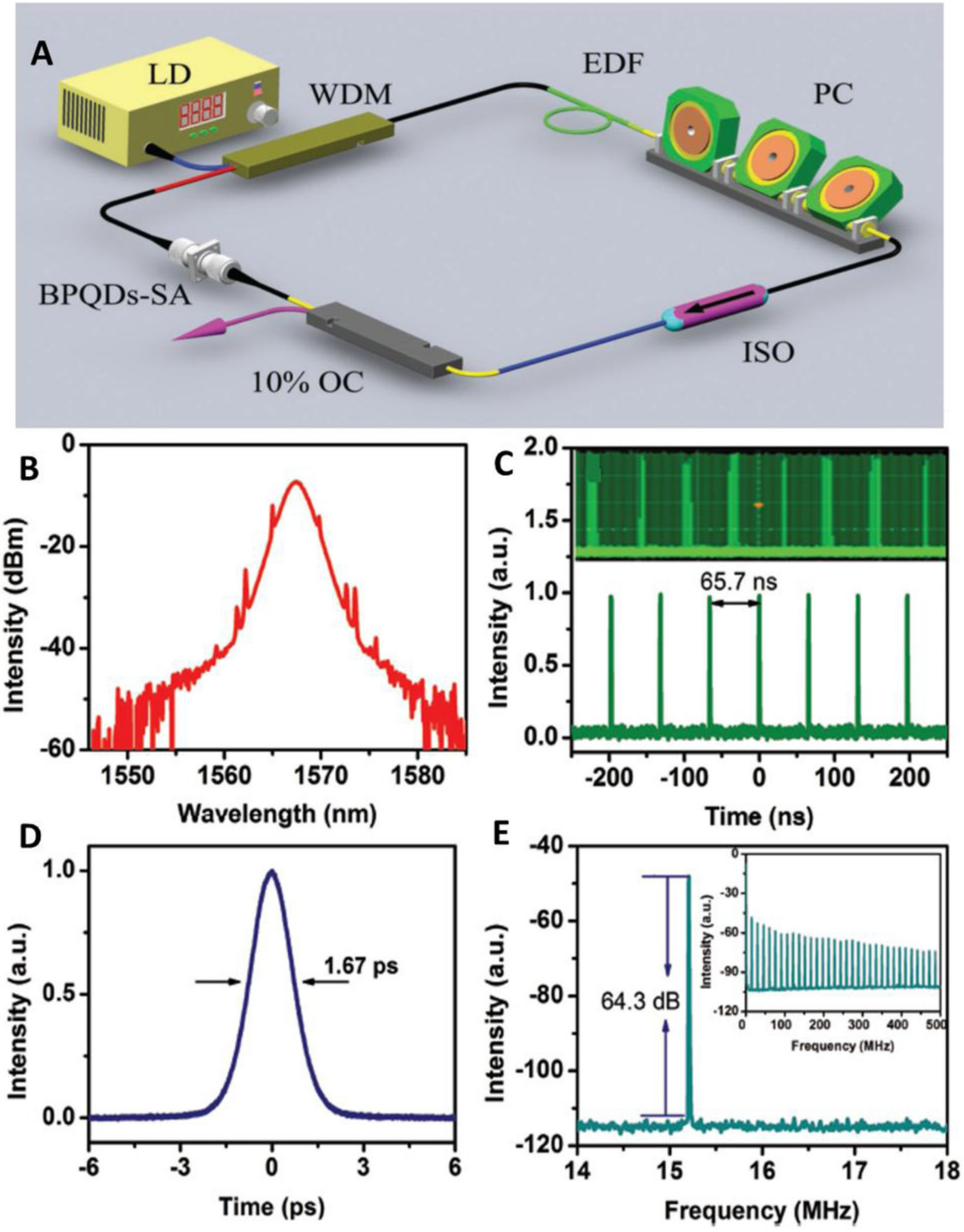

Fig. 20. (A) The schematic illustration of the incorporation of BPQDs saturable absorber into passively mode-locked fiber laser. LD: laser diode. EDF: erbium-doped fiber. PC: polarization controller. PC: polarization controller. ISO: polarization independent isolator. OC: output coupler. BPQDs-SA: BPQDs based saturable absorber. (B) Obtained optical spectrum. (C) Corresponding pulse train. (D) Autocorrelation trace. (E) The radio frequency spectrum (inset: the wideband RF spectrum) of the mode-locked pulses [117]. Copyright © 2016 WILEY-VCH Verlag GmbH & Co. KGaA, Weinheim.

which requires large surface area for electrosorption of ions. Hao et al. reported the use of restacked liquid-exfoliated BP flakes as flexible electrodes in all-solid-state supercapacitor (ASSP) [101]. The schematic cross-section of the BP-ASSP is shown in inset of Fig. 16A. The BP flakes were drop-casted on Pt-coated PET substrates and a gel electrolyte PVA/H_3PO_4 was sandwiched between two BP films. The BP-ASSP delivered a high capacitance up to 13.75 F cm^{-3} at a scan rate of 0.01 V s^{-1} (Fig. 16A). The Galvanostatic charge/discharge curves displayed dominant EDLC behavior of the BP flakes (Fig. 16B). Remarkably, the BP-ASSP demonstrated outstanding mechanical flexibility and cycling stability over 30,000 cycles (Fig. 16C). The Ragone plot (Fig. 16D) shows the superior performance of the BP-ASSP as compared to several commercial energy-storage systems and reported devices. The results indicate that liquid-exfoliated BP flakes are promising as flexible electrode material for high performance energy-storage systems.

BPQDs

Despite being the most stable allotrope of phosphorus, BP is still sensitive to oxygen and moisture. Therefore, it seems to be a challenge to synthesize, characterize, and apply pristine BPQDs to tra-

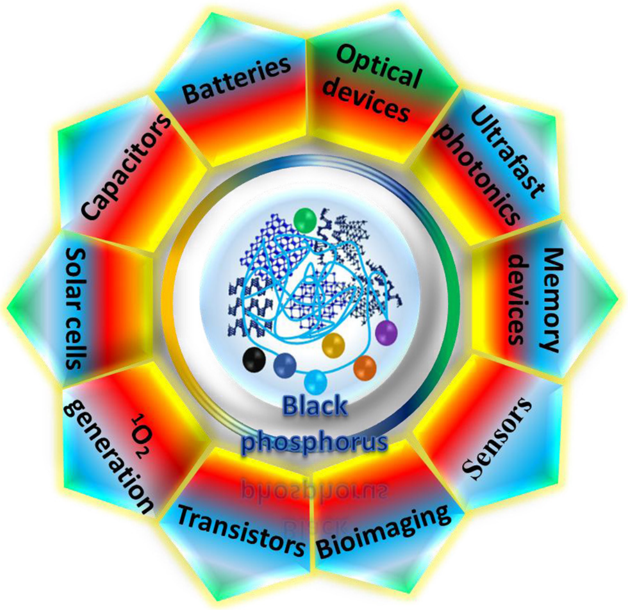

Fig. 21. Schematic illustration of the applications of liquid-phase exfoliated BP and its interrelationship between the environment and energy conversion towards achieving sustainability.

ditional electronic devices, e.g., FET. But BPQDs can be potentially applied in the energy devices, such as Li-ion or Na-ion batteries which operated under the conditions free of water and oxygen. On the other hand, BPQDs can be functionalized by other materials, such as polyethylene glycol-amine (PEG-NH_2), to enhance the disperse stability in water [70]. In addition to pristine BPQDs, oxidation of BPQDs may provide the opportunity to tailor their electronic and optical properties for different applications [102]. Generally, we can deeply understand the properties of BPQDs through extending and investigating their applications in many diverse fields, e.g., sensor, bio-imaging, solar cell, energy storage, ultrafast photonics.

Humidity sensor and memory devices

Humidity means the presence of water in the air. The amount of water vapor in air can affect human comfort as well as many industrial manufacturing processes. The presence of water vapor also influences physical, chemical, and biological processes. Therefore, humidity sensing seems to be very important, especially in the control systems for industrial processes and human comfort. Recently, Zhu et al. [71] demonstrated that BPQDs showed great potential in the application of highly sensitive humidity sensor. Apart from the application of BPQDs for cancer treatment through photothermal heating of BPQDs in water (with a broad absorption in the NIR band as shown in Fig. 17), BPQD film was also successfully incorporated into an interdigital resistive humidity sensor. The sensing resistance data with respect to relative humidity (RH) at ∼21 °C showed that the resistance of the BPQD-based sensor decreases by ∼4 orders of magnitude as the RH varies from 10% to 90%, which displayed the highest value for humidity detection in the current literatures [103,104]. Namely, the BPQDs outperform the BP flakes with respect to humidity sensor. Moreover, the stability of BPQD-based humidity sensor was further examined over a prolonged period of ambient exposure for 66 h. It can be found there is a slight change in the results of the humidity sensor in prolonged exposure to 35% and 90% RH at 21 °C, implying highly stable and sensitive of BPQD-based sensor.

Besides the application in humidity sensor, BPQDs can also reveal a unique conductance-switching effect by forming BPQD-PVP hybrid nanomaterials, indicating its potential application in data storage devices [69]. As shown in Fig. 18, the BPQD-PVP based device exhibits a flash memory effect with a high on/off current ratio of more than 6.0×10^4 and good stability obtained at the reading voltage of 0.2 V, which is significantly higher than that of C60-PVP, MoS_2-PVP and Au nanoparticle/ZnO nanorod-PVP based diodes [69], implying its superior performance as a flexible memory device.

Biomedical applications

Since the group of Bruchez and Nie reported the use of QDs in the detection of biological targets in 1998 [105,106] a series of QD-based fluorescent biosensors have been developed for protein and nucleic acid detection [107,108]. The use of QDs as an effective tool for cellular labelling and *in vivo* imaging has also become more and more realistic through the improvement of their stability and biocompatibility. However, the synthesis of QDs usually results in surface-bound organic nonpolar ligands that are not biocompatible, requiring the surface modification of the QDs. Rosenthal et al. reported surface modification of QDs could be done through ligand exchange [109]. Usually, QDs can be functionalized with terminating groups on surface ligands, such as carboxylic acid, azide, amine or streptavidin/avidin protein. These well characterized constructs allow for cellular labeling by using antibodies [110], peptides/proteins [111,112] or sugars [113] in fixed and unfixed cell and tissue cultures.

Recently, BP has shown great potential in the NIR bio-medical applications due to its direct bandgap of 0.3–2 eV. The reported photothermal properties of BPQDs obviously displayed an excellent NIR photothermal performance and biocompatibility [70] through the stable dispersion of BPQDs in water realized by functionalizing with PEG-NH_2. The photothermal effect of the BPQDs in cancer cells was directly investigated as shown in Fig. 19. The C6 and MCF7 cancer cells were incubated with the BPQDs (with size of 2.6 ± 1.8 nm) for four hours, and then were illuminated with a NIR laser (808 nm, 1.0 W/cm) for 10 min. The results revealed that almost all of the cells incubated with only 50 ppm of the PEG-modified BPQDs were killed, but those incubated in the absence of BPQDs stay alive, when exposed to the NIR laser. Furthermore, the BPQDs showed no dark toxicity to these cells at concentration between 20 and 200 ppm. As for the larger size BPQDs with an average diameter of 10 nm, they showed no or little cytotoxic cell-viability effects in vitro involving blue- and green-fluorescence cell imaging, [114] revealing their potential applications in drug delivery or cellular tracking systems. These results demonstrate good photothermal therapy efficiency of BPQDs in promoting cancer cell death by facilitating their cellular internalization into cancer cells due to their ultrasmall size of 2.6 ± 1.8 nm [70]. Besides, biodegradable BPQDs/PLGA (poly (lactic-co-glycolic acid)) nanospheres have been experimentally demonstrated to show great potential applications for *in vivo* photothermal cancer therapy, [115] revealing its promising for in *vivo* imaging.

Ultrafast photonics

Light-matter interaction at the interfaces of van der Waals solids is the key to build high-performance optoelectronic devices, e.g., the strong enhancement of light-matter interaction and the formation of microcavity polaritons in MoS_2 for the development of practical polaritonic circuits and switches [116]. QDs are nanoscale semiconductor devices that tightly confine either electrons or holes in all three spatial dimensions, which exhibit unique electronic and optical properties, distinguished from its bulk form, in association with the quantum confinement and edge effects. However, the light-matter interaction between laser and BPQDs, and the ultrafast and nonlinear optical properties of BPQDs have rarely been studied. Recently, Xu et al. [117] demonstrated that BPQDs prepared by liquid-phase exfoliation in NMP showed excellent nonlinear optical saturable absorption (as shown in Fig. 20) with a modulation depth of 36% and a saturable intensity of ~3.3 GW cm^{-2} through performing femto-second Z-scan measurement. The central spectrum of the mode-locked pulse showed a 3 dB spectral bandwidth of 2.4 nm and the oscilloscope trace of the output pulse-train with a pulse-to-pulse interval of 65.7 ns. The noise ratio of electrical signal at 15.25 MHz can be even up to ~64.3 dB measured with 10 Hz resolution bandwidth. These saturable absorption properties of BPQDs are better than that of other QDs, such as PbS [118], Fe_2O_3 [119], GaAs [120], which enables the design of a novel optical saturable absorber to deliver the generated ultrashort pulse at a wavelength of 1567.5 nm in an Er-doped fiber laser. These findings suggest BPQDs can be developed as a good candidate for ultrafast photonic devices, giving a good platform for investigating the light-QDs interaction and offering an evidence for improving the current knowledge.

Conclusions and outlooks

The search for 2D materials is an ongoing process and has received significant attention all over the world in recent years because of their extraordinary chemical, mechanical and physical properties. One typical way for exploring the properties of 2D materials is to develop growth methods for 2D materials. Liquid-phase exfoliation of 2D materials, classified into the so-called top-down strategy, is a usual and high-efficiency technique to achieve high-quality large surface area nanosheets with high yields and without large number of defects. As for the production of single- and few-layer 2D nanomaterials in liquid environments for advanced applications, an efficient exfoliation method is required by balancing the surface tensions (combined with Hansen solubility parameter) between the solvents and 2D materials. Recently, the development of new strategies to exfoliate 2D materials in polar solvents with the aid of sonication have opened a great range of possibilities to produce 2D nanosheets and QDs not only as nanofillers in composite materials but also in applications at the nanoscale for sensors, solar cells, energy storage, electronic devices, optical devices or bio-imaging.

In this review, we mainly discussed the structural and fundamental properties of BP, and the recent advances of liquid-phase exfoliation of BP and its applications. With the aid of ultrasonication, scalable production of BP flakes and QDs can be realized and their applications can be extended from nanoelectronics to biotechnology. Meanwhile, layered BP material reveals to be compatible with other 2D materials to form heterostructures, which seems to have strong light-matter coupling and to exhibit potential photocatalytic effect. As a whole, the relationship of the environment, energy conversion and human beings can be pictorially depicted in Fig. 21 as a mind map to all the readers for the state-of-the-art research in liquid-phase exfoliated BP flakes and QDs.

Accordingly, searching for new approaches to avoid surface degradation is a key problem and a challenge for achieving high performance BP-based electronic devices. For example, BP surface is usually passivated by a protective layer, such as Al_2O_3, to avoid etching by the water in air. However, BP still degrades as the time goes when exposed to the air. Recently, in contrast of passivation by a top layer on BP surface, covalent aryl diazonium functionalization can suppresses the chemical degradation of exfoliated BP even after three weeks of ambient exposure, [72] which opens a new way to increase the stability of exfoliated BP through functionalizing the surface to tailor their chemical, optical and electronic properties. Therefore, the surface modification strategy will be a future direction for achieving desirable outcomes of BP and other 2D system.

For practical applications, commercial electronic devices based on 2D materials usually need large area film. Although some strategies have been put forward, such as PLD (pulse laser deposition) [24] for amorphous BP film, conversion of red phosphorus film into BP [23], their stability and continuity still are the existing problems. Due to its high-pressure condition for growing BP bulk, CVD with high-pressure might be a possible technique for preparing large-area high-quality BP film [42]. In addition, large-area thick mechanically exfoliated BP flakes can be thermally thinned down to ultrathin BP film, which is similar to the thermal thinning of MoS_2 [121] and might further draw scientific attention.

Accompanied with its high absorbance, direct and narrow band gap, and effective harvest of low energy photons, BP also reveals potential applications for photocatalysis though its high probability of radiative recombination of photo-excited electron–hole pairs [92]. Alternatively, tuning the band-edge positions of BP by forming BP/other 2D materials (like BP/WS_2, BP/C_3N_4) heterostructures could be another approach to improve the feasibility of BP-based photocatalyst. Compared with metal-free graphitic carbon nitride for water splitting, BPQDs combined with C_3N_4 might be applied to water splitting. Meanwhile, BPQDs will be also a potential choice as a transport layer or even active layer in organic solar cells or incorporated into perovskite solids to form LED or hybrid solar cell.

Apart from BP/graphene based batteries, other heterostructures like BP/BPQDs, BP/RGO (reduced graphene oxide), BPQDs/graphene, BPQDs/RGO, BPQDs/CNT (carbon nanotube) will be another direction for high performance BP-based sodium or Li-ion batteries.

Generally, we believe that the research on the applications of liquid-phase exfoliated BP flakes or BPQDs will attract significant attention world-wide. Liquid-phase exfoliation process will become more important for 2D materials without CVD.

Acknowledgements

S. H. Lin and Y. S. Chui are contributed equally. This work was financially supported by the PolyU grants (1-ZE14 and 1-ZVGH) and the Research Grants Council (RGC) of Hong Kong (Project No. PolyU 153030/15P).

References

[1] K.S. Novoselov, A.K. Geim, S.V. Morozov, D. Jiang, Y. Zhang, S.V. Dubonos, I.V. Grigorieva, A.A. Firsov, Science 306 (2004) 666.
[2] A.K. Geim, K.S. Novoselov, Nat. Mater. 6 (2007) 183–191.
[3] Y. Liu, X. Dong, P. Chen, Chem. Soc. Rev. 41 (2012) 2283–2307.
[4] X. Wang, G. Sun, P. Routh, D.-H. Kim, W. Huang, P. Chen, Chem. Soc. Rev. 43 (2014) 7067–7098.
[5] F. Bonaccorso, L. Colombo, G. Yu, M. Stoller, V. Tozzini, A.C. Ferrari, R.S. Ruoff, V. Pellegrini, Science 347 (2015).
[6] M.K. Chini, S. Chatterjee, FlatChem 1 (2017) 1–5.
[7] C.N.R. Rao, H.S.S. Ramakrishna Matte, U. Maitra, Angew. Chem. Int. Ed. 52 (2013) 13162–13185.
[8] R. Ma, T. Sasaki, Acc. Chem. Res. 48 (2015) 136–143.
[9] V. Nicolosi, M. Chhowalla, M.G. Kanatzidis, M.S. Strano, J.N. Coleman, Science 340 (2013).
[10] Z.-H. Liu, K. Ooi, H. Kanoh, W.-P. Tang, T. Tomida, Langmuir 16 (2000) 4154–4164.
[11] S. Lin, S. Liu, Z. Yang, Y. Li, T.W. Ng, Z. Xu, Q. Bao, J. Hao, C.-S. Lee, C. Surya, F. Yan, S.P. Lau, Adv. Func. Mater. 26 (2016) 864–871.
[12] A. Politano, M.S. Vitiello, L. Viti, D.W. Boukhvalov, G. Chiarello, FlatChem 1 (2017) 60–64.
[13] K.F. Mak, C. Lee, J. Hone, J. Shan, T.F. Heinz, Phys. Rev. Lett. 105 (2010) 136805.
[14] J. Feng, X. Qian, C.-W. Huang, J. Li, Nat. Photon. 6 (2012) 866–872.
[15] M. Fontana, T. Deppe, A.K. Boyd, M. Rinzan, A.Y. Liu, M. Paranjape, P. Barbara, Sci. Rep. 3 (2013) 1634.
[16] M. Bernardi, M. Palummo, J.C. Grossman, Nano Lett. 13 (2013) 3664–3670.

[17] Z. Yin, H. Li, H. Li, L. Jiang, Y. Shi, Y. Sun, G. Lu, Q. Zhang, X. Chen, H. Zhang, ACS Nano 6 (2012) 74–80.

[18] H.S. Lee, S.-W. Min, Y.-G. Chang, M.K. Park, T. Nam, H. Kim, J.H. Kim, S. Ryu, S. Im, Nano Lett. 12 (2012) 3695–3700.

[19] Y. Ye, Z. Ye, M. Gharghi, H. Zhu, M. Zhao, X. Yin, X. Zhang, arXiv 1305 (2013) 4235.

[20] L. Li, Y. Yu, G.J. Ye, Q. Ge, X. Ou, H. Wu, D. Feng, X.H. Chen, Y. Zhang, Nat. Nano 9 (2014) 372–377.

[21] A.S. Rodin, A. Carvalho, A.H. Castro Neto, Phys. Rev. Lett. 112 (2014) 176801.

[22] S. Das, W. Zhang, M. Demarteau, A. Hoffmann, M. Dubey, A. Roelofs, Nano Lett. 14 (2014) 5733–5739.

[23] L. Xuesong, D. Bingchen, W. Xiaomu, C. Sizhe, V. Michelle, K. Shun-ichiro, P. Grace, L. Minjoo Larry, C. Judy, W. Han, X. Fengnian, 2D Mater 2 (2015) 031002.

[24] Z. Yang, J. Hao, S. Yuan, S. Lin, H.M. Yau, J. Dai, S.P. Lau, Adv. Mater. 27 (2015) 3748–3754.

[25] X. Chen, Y. Wu, Z. Wu, Y. Han, S. Xu, L. Wang, W. Ye, T. Han, Y. He, Y. Cai, N. Wang, Nat. Commun. 6 (2015) 7315.

[26] L. Gen, X. Shuigang, S. Junying, H. Jianqiang, W. Zefei, H. Tianyi, L. Jiangxiazi, W. Wing Ki, C. Yuan, L. Rolf, W. Ning, 2D Mater 3 (2016) 031001.

[27] J.S. Kim, P.J. Jeon, J. Lee, K. Choi, H.S. Lee, Y. Cho, Y.T. Lee, D.K. Hwang, S. Im, Nano Lett. 15 (2015) 5778–5783.

[28] J. Na, Y.T. Lee, J.A. Lim, D.K. Hwang, G.-T. Kim, W.K. Choi, Y.-W. Song, ACS Nano 8 (2014) 11753–11762.

[29] Y. Li, Z. Hu, S. Lin, S.K. Lai, W. Ji, S.P. Lau, Adv. Func. Mater. (2016), http://dx.doi.org/10.1002/adfm.201600986.

[30] H. Liu, Y. Du, Y. Deng, P.D. Ye, Chem. Soc. Rev. 44 (2015) 2732–2743.

[31] G. Konstantatos, I. Howard, A. Fischer, S. Hoogland, J. Clifford, E. Klem, L. Levina, E.H. Sargent, Nature 442 (2006) 180–183.

[32] D. Huang, T.A. Webb, C.-L. Song, C.-Z. Chang, J.S. Moodera, E. Kaxiras, J.E. Hoffman, Nano Lett. 16 (2016) 4224–4229.

[33] F. Wang, W.K.H. Ng, J.C. Yu, H. Zhu, C. Li, L. Zhang, Z. Liu, Q. Li, Appl. Catal. B: Environ. 111–112 (2012) 409–414.

[34] <https://en.wikipedia.org/wiki/Phosphorus>.

[35] A. Morita, Appl. Phys. A 39 (1986) 227–242.

[36] J. Wu, N. Mao, L. Xie, H. Xu, J. Zhang, Angew. Chem. Int. Ed. 54 (2015) 2366–2369.

[37] K.T. Lam, Z. Dong, J. Guo, IEEE Electr. Dev. Lett. 35 (2014) 963–965.

[38] J.C. Jamieson, Science 139 (1963) 1291–1292.

[39] S. Minomura, H.P.I.o. Japan, Solid State Physics Under Pressure: Recent Advances with Anvil Devices, KTK Scientific Publishers, 1985.

[40] J.K. Burdett, S. Lee, J. Solid State Chem. 44 (1982) 415–424.

[41] S.M. Clark, J.M. Zaug, Phys. Rev. B 82 (2010) 134111.

[42] S. Lin, Y. Li, W. Lu, Y.S. Chui, L. Rogée, Q. Bao, S.P. Lau, 2D Mater 4 (2017) 025001.

[43] H. Yuan, X. Liu, F. Afshinmanesh, W. Li, G. Xu, J. Sun, B. Lian, A.G. Curto, G. Ye, Y. Hikita, Z. Shen, S.-C. Zhang, X. Chen, M. Brongersma, H.Y. Hwang, Y. Cui, Nat. Nano 10 (2015) 707–713.

[44] Y. Cai, G. Zhang, Y.-W. Zhang, Sci. Rep. 4 (2014) 6677.

[45] C.Q. Han, M.Y. Yao, X.X. Bai, L. Miao, F. Zhu, D.D. Guan, S. Wang, C.L. Gao, C. Liu, D. Qian, Y. Liu, J.-F. Jia, Phys. Rev. B 90 (2014) 085101.

[46] V. Tran, R. Soklaski, Y. Liang, L. Yang, Phys. Rev. B 89 (2014) 235319.

[47] Y. Takao, H. Asahina, A. Morita, J. Phys. Soc. Jpn. 50 (1981) 3362–3369.

[48] Z.S. Popović, J.M. Kurdestany, S. Satpathy, Phys. Rev. B 92 (2015) 035135.

[49] K.S. Suslick, Science 247 (1990) 1439–1445.

[50] J.N. Coleman, M. Lotya, A. O'Neill, S.D. Bergin, P.J. King, U. Khan, K. Young, A. Gaucher, S. De, R.J. Smith, I.V. Shvets, S.K. Arora, G. Stanton, H.-Y. Kim, K. Lee, G.T. Kim, G.S. Duesberg, T. Hallam, J.J. Boland, J.J. Wang, J.F. Donegan, J.C. Grunlan, G. Moriarty, A. Shmeliov, R.J. Nicholls, J.M. Perkins, E.M. Grieveson, K. Theuwissen, D.W. McComb, P.D. Nellist, V. Nicolosi, Science 331 (2011) 568–571.

[51] J.N. Coleman, Adv. Func. Mater. 19 (2009) 3680–3695.

[52] Y. Zhang, H. Wang, Z. Luo, H.T. Tan, B. Li, S. Sun, Z. Li, Y. Zong, Z.J. Xu, Y. Yang, K.A. Khor, Q. Yan, Adv. Energy Mater. 6 (2016), 1600453-n/a.

[53] J.R. Brent, N. Savjani, E.A. Lewis, S.J. Haigh, D.J. Lewis, P. O'Brien, Chem. Commun. 50 (2014) 13338–13341.

[54] J. Kang, J.D. Wood, S.A. Wells, J.-H. Lee, X. Liu, K.-S. Chen, M.C. Hersam, ACS Nano 9 (2015) 3596–3604.

[55] H. Mu, S. Lin, Z. Wang, S. Xiao, P. Li, Y. Chen, H. Zhang, H. Bao, S.P. Lau, C. Pan, D. Fan, Q. Bao, Adv. Opt. Mater. 3 (2015) 1447–1453.

[56] D. Hanlon, C. Backes, E. Doherty, C.S. Cucinotta, N.C. Berner, C. Boland, K. Lee, A. Harvey, P. Lynch, Z. Gholamvand, S. Zhang, K. Wang, G. Moynihan, A. Pokle, Q.M. Ramasse, N. McEvoy, W.J. Blau, J. Wang, G. Abellan, F. Hauke, A. Hirsch, S. Sanvito, D.D. O'Regan, G.S. Duesberg, V. Nicolosi, J.N. Coleman, Nat. Commun. 6 (2015) 8563.

[57] A.H. Woomer, T.W. Farnsworth, J. Hu, R.A. Wells, C.L. Donley, S.C. Warren, ACS Nano 9 (2015) 8869–8884.

[58] J. Kang, S.A. Wells, J.D. Wood, J.-H. Lee, X. Liu, C.R. Ryder, J. Zhu, J.R. Guest, C.A. Husko, M.C. Hersam, Proc. Nat. Acad. Sci. 113 (2016) 11688–11693.

[59] J. Liu, R.H. Hurt, Environ. Sci. Technol. 44 (2010) 2169–2175.

[60] A. O'Neill, U. Khan, P.N. Nirmalraj, J. Boland, J.N. Coleman, J. Phys. Chem. C 115 (2011) 5422–5428.

[61] G. Cunningham, M. Lotya, C.S. Cucinotta, S. Sanvito, S.D. Bergin, R. Menzel, M. S.P. Shaffer, J.N. Coleman, ACS Nano 6 (2012) 3468–3480.

[62] W. Zhao, Z. Xue, J. Wang, J. Jiang, X. Zhao, T. Mu, ACS Appl. Mater. Interfaces 7 (2015) 27608–27612.

[63] Z. Congyan, Y. Ming, A. George, D. Ruchira Ravinath, S. Gamini, Nanotechnology 28 (2017) 075401.

[64] C.-J. Shih, S. Lin, M.S. Strano, D. Blankschtein, J. Am. Chem. Soc. 132 (2010) 14638–14648.

[65] A. Favron, E. Gaufres, F. Fossard, A.-L. Phaneuf-Lheureux, N.Y.W. Tang, P.L. Levesque, A. Loiseau, R. Leonelli, S. Francoeur, R. Martel, Nat. Mater. 14 (2015) 826–832.

[66] H. Wang, X. Yang, W. Shao, S. Chen, J. Xie, X. Zhang, J. Wang, Y. Xie, J. Am. Chem. Soc. 137 (2015) 11376–11382.

[67] J. Kang, J.-W.T. Seo, D. Alducin, A. Ponce, M.J. Yacaman, M.C. Hersam, Nat. Commun. 5 (2014) 5478.

[68] N. Wei, C. Lv, Z. Xu, Langmuir 30 (2014) 3572–3578.

[69] X. Zhang, H. Xie, Z. Liu, C. Tan, Z. Luo, H. Li, J. Lin, L. Sun, W. Chen, Z. Xu, L. Xie, W. Huang, H. Zhang, Angew. Chem. Int. Ed. 54 (2015) 3653–3657.

[70] Z. Sun, H. Xie, S. Tang, X.-F. Yu, Z. Guo, J. Shao, H. Zhang, H. Huang, H. Wang, P. K. Chu, Angew. Chem. Int. Ed. 54 (2015) 11526–11530.

[71] C. Zhu, F. Xu, L. Zhang, M. Li, J. Chen, S. Xu, G. Huang, W. Chen, L. Sun, Chem. – A Eur. J. 22 (2016) 7357–7362.

[72] C.R. Ryder, J.D. Wood, S.A. Wells, Y. Yang, D. Jariwala, T.J. Marks, G.C. Schatz, M.C. Hersam, Nat. Chem. 8 (2016) 597–602.

[73] D. Yue, D. Lee, Y.D. Jang, M.S. Choi, H.J. Nam, D.-Y. Jung, W.J. Yoo, Nanoscale 8 (2016) 12773–12779.

[74] H. Liu, A.T. Neal, Z. Zhu, Z. Luo, X. Xu, D. Tománek, P.D. Ye, ACS Nano 8 (2014) 4033–4041.

[75] M. Buscema, D.J. Groenendijk, S.I. Blanter, G.A. Steele, H.S.J. van der Zant, A. Castellanos-Gomez, Nano Lett. 14 (2014) 3347–3352.

[76] M. Buscema, D.J. Groenendijk, G.A. Steele, H.S.J. van der Zant, A. Castellanos-Gomez, Nat. Commun. 5 (2014) 4651.

[77] D.V. Talapin, C.B. Murray, Science 310 (2005) 86–89.

[78] P. Yasaei, B. Kumar, T. Foroozan, C. Wang, M. Asadi, D. Tuschel, J.E. Indacochea, R.F. Klie, A. Salehi-Khojin, Adv. Mater. 27 (2015) 1887–1892.

[79] H. Kaur, S. Yadav, A.K. Srivastava, N. Singh, J.J. Schneider, O.P. Sinha, V.V. Agrawal, R. Srivastava, Sci. Rep. 6 (2016) 34095.

[80] Y. Chen, G. Jiang, S. Chen, Z. Guo, X. Yu, C. Zhao, H. Zhang, Q. Bao, S. Wen, D. Tang, D. Fan, Opt. Express 23 (2015) 12823–12833.

[81] Y. Wang, G. Huang, H. Mu, S. Lin, J. Chen, S. Xiao, Q. Bao, J. He, Appl. Phys. Lett. 107 (2015) 091905.

[82] H. Shi, R. Yan, S. Bertolazzi, J. Brivio, B. Gao, A. Kis, D. Jena, H.G. Xing, L. Huang, ACS Nano 7 (2013) 1072–1080.

[83] Q. Wang, S. Ge, X. Li, J. Qiu, Y. Ji, J. Feng, D. Sun, ACS Nano 7 (2013) 11087–11093.

[84] D. Ravelli, D. Dondi, M. Fagnoni, A. Albini, Chem. Soc. Rev. 38 (2009) 1999–2011.

[85] M.Z. Rahman, C.W. Kwong, K. Davey, S.Z. Qiao, Energy Environ. Sci. 9 (2016) 709–728.

[86] J. Ran, J. Zhang, J. Yu, M. Jaroniec, S.Z. Qiao, Chem. Soc. Rev. 43 (2014) 7787–7812.

[87] J.R. Bolton, S.J. Strickler, J.S. Connolly, Nature 316 (1985) 495–500.

[88] C.R. Dean, A.F. Young, I. Meric, C. Lee, L. Wang, S. Sorgenfrei, K. Watanabe, T. Taniguchi, P. Kim, K.L. Shepard, J. Hone, Nat. Nano. 5 (2010) 722–726.

[89] B. Sa, Y.-L. Li, J. Qi, R. Ahuja, Z. Sun, J. Phys. Chem. C 118 (2014) 26560–26568.

[90] J. Hu, Z. Guo, P.E. McWilliams, J.E. Darges, D.L. Druffel, A.M. Moran, S.C. Warren, Nano Lett. 16 (2016) 74–79.

[91] H. Uk Lee, S.C. Lee, J. Won, B.-C. Son, S. Choi, Y. Kim, S.Y. Park, H.-S. Kim, Y.-C. Lee, J. Lee, Sci. Rep. 5 (2015) 8691.

[92] X. Zhu, T. Zhang, Z. Sun, H. Chen, J. Guan, X. Chen, H. Ji, P. Du, S. Yang, Adv. Mater. (2017), 1605776-n/a.

[93] H. Guo, N. Lu, J. Dai, X. Wu, X.C. Zeng, J. Phys. Chem. C 118 (2014) 14051–14059.

[94] Y.-P. Yuan, L.-W. Ruan, J. Barber, S.C. Joachim Loo, C. Xue, Energy Environ. Sci. 7 (2014) 3934–3951.

[95] J.E. Padilha, A. Fazzio, A.J.R. da Silva, Phys. Rev. Lett. 114 (2015) 066803.

[96] W. Tao, X. Zhu, X. Yu, X. Zeng, Q. Xiao, X. Zhang, X. Ji, X. Wang, J. Shi, H. Zhang, L. Mei, Adv. Mater. 29 (2017), 1603276-n/a.

[97] J. Sun, G. Zheng, H.-W. Lee, N. Liu, H. Wang, H. Yao, W. Yang, Y. Cui, Nano Lett. 14 (2014) 4573–4580.

[98] J. Sun, H.-W. Lee, M. Pasta, H. Yuan, G. Zheng, Y. Sun, Y. Li, Y. Cui, Nat. Nano 10 (2015) 980–985.

[99] C.M. Park, H.J. Sohn, Adv. Mater. 19 (2007) 2465–2468.

[100] L. Chen, G. Zhou, Z. Liu, X. Ma, J. Chen, Z. Zhang, X. Ma, F. Li, H.-M. Cheng, W. Ren, Adv. Mater. 28 (2016) 510–517.

[101] C. Hao, B. Yang, F. Wen, J. Xiang, L. Li, W. Wang, Z. Zeng, B. Xu, Z. Zhao, Z. Liu, Y. Tian, Adv. Mater. 28 (2016) 3194–3201.

[102] G. Wang, R. Pandey, S.P. Karna, Nanoscale 7 (2015) 524–531.

[103] S. Borini, R. White, D. Wei, M. Astley, S. Haque, E. Spigone, N. Harris, J. Kivioja, T. Ryhänen, ACS Nano 7 (2013) 11166–11173.

[104] P. Yasaei, A. Behranginia, T. Foroozan, M. Asadi, K. Kim, F. Khalili-Araghi, A. Salehi-Khojin, ACS Nano 9 (2015) 9898–9905.

[105] W.C.W. Chan, S. Nie, Science 281 (1998) 2016–2018.

[106] M. Bruchez, M. Moronne, P. Gin, S. Weiss, A.P. Alivisatos, Science 281 (1998) 2013–2016.

[107] Q. Ma, X. Su, Analyst 136 (2011) 4883–4893.

[108] W. Miao, Chem. Rev. 108 (2008) 2506–2553.

[109] S.J. Rosenthal, I. Tomlinson, E.M. Adkins, S. Schroeter, S. Adams, L. Swafford, J. McBride, Y. Wang, L.J. DeFelice, R.D. Blakely, J. Am. Chem. Soc. 124 (2002) 4586–4594.

[110] B. Biermann, S. Sokoll, J. Klueva, M. Missler, J.S. Wiegert, J.B. Sibarita, M. Heine, Nat. Commun. 5 (2014) 3024.
[111] X. Wu, H. Liu, J. Liu, K.N. Haley, J.A. Treadway, J.P. Larson, N. Ge, F. Peale, M.P. Bruchez, Nat. Biotech. 21 (2003) 41–46.
[112] W. Cai, X. Chen, Nat. Protocol. 3 (2008) 89–96.
[113] C.-T. Chen, Y.S. Munot, S.B. Salunke, Y.-C. Wang, R.-K. Lin, C.-C. Lin, C.-C. Chen, Y.H. Liu, Adv. Func. Mater. 18 (2008) 527–540.
[114] H.U. Lee, S.Y. Park, S.C. Lee, S. Choi, S. Seo, H. Kim, J. Won, K. Choi, K.S. Kang, H. G. Park, H.-S. Kim, H.R. An, K.-H. Jeong, Y.-C. Lee, J. Lee, Small 12 (2016) 214–219.
[115] J. Shao, H. Xie, H. Huang, Z. Li, Z. Sun, Y. Xu, Q. Xiao, X.-F. Yu, Y. Zhao, H. Zhang, H. Wang, P.K. Chu, Nat. Commun. 7 (2016) 12967.
[116] X. Liu, T. Galfsky, Z. Sun, F. Xia, E.-C. Lin, Y.-H. Lee, S. Kéna-Cohen, V.M. Menon, Nat. Photon. 9 (2015) 30–34.
[117] Y. Xu, Z. Wang, Z. Guo, H. Huang, Q. Xiao, H. Zhang, X.-F. Yu, Adv. Opt. Mater. 4 (2016) 1223–1229.
[118] B. Yu, G. Yin, C. Zhu, F. Gan, Opt. Mater. 11 (1998) 17–21.
[119] B. Yu, C. Zhu, F. Gan, X. Wu, G. Zhang, G. Tang, W. Chen, Opt. Mater. 8 (1997) 249–254.
[120] B.L. Justus, R.J. Tonucci, A.D. Berry, Appl. Phys. Lett. 61 (1992) 3151–3153.
[121] J. Wu, H. Li, Z. Yin, H. Li, J. Liu, X. Cao, Q. Zhang, H. Zhang, Small 9 (2013) 3314–3319.